Tribology Letters (2024) 72:92
https://doi.org/10.1007/s11249-024-01894-w

ORIGINAL PAPER

Elastohydrodynamic Traction and Film Thickness at High Speeds

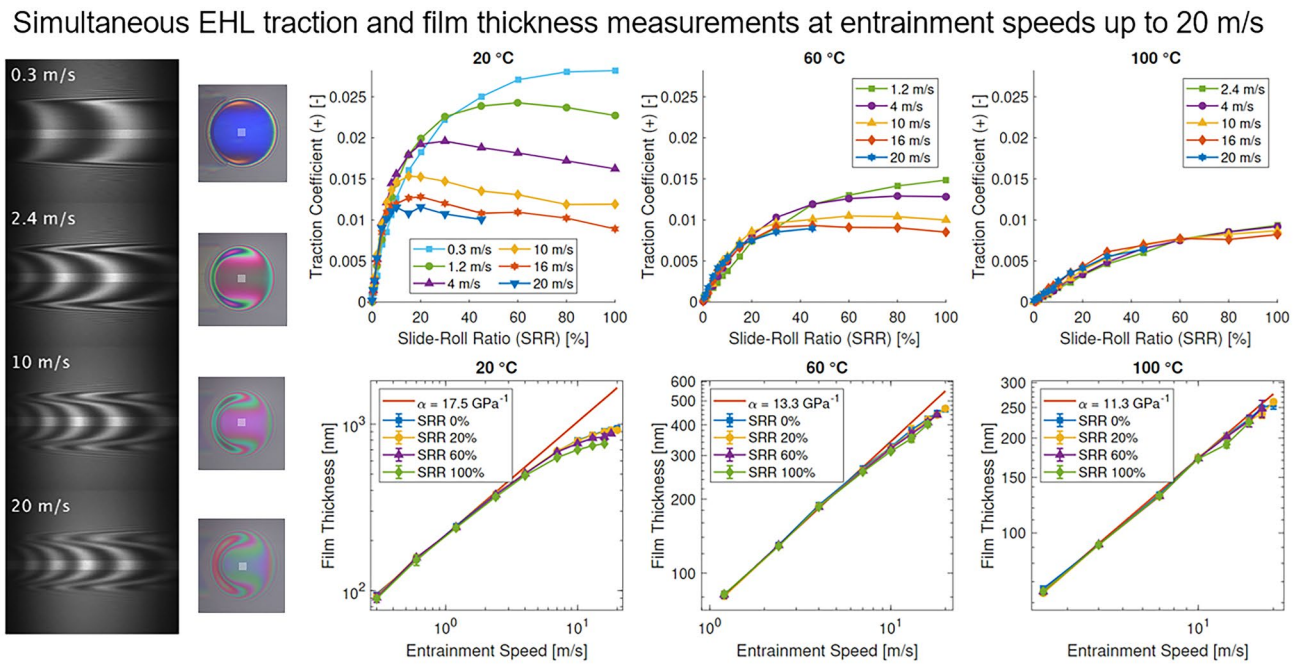
Alexander MacLaren[1] · **Amir Kadiric**[1]

Received: 9 March 2024 / Accepted: 9 July 2024 / Published online: 18 July 2024
© The Author(s) 2024, corrected publication 2024

Abstract

A renewed interest in elastohydrodynamic lubrication (EHL) phenomena at high speeds, for which thermal effects strongly influence both traction and film thickness, has grown out of the challenges presented by high-speed geared transmissions in electric vehicles. This study uses a new ball-on-disc set-up employing the well-known ultra-thin-film interferometry technique to simultaneously measure EHL film thickness and traction at entrainment speeds up to 20 m/s and slide-roll ratios up to 100%. The effect of fluid composition is examined for Group I, II and III mineral oils, for two polyalphaolefins in Group IV, and for the traction fluid Santotrac 50. The effect of viscosity in the range 4–180 mPa.s is investigated by varying bulk fluid temperature. At high speeds, both film thickness and traction are considerably lower than predicted by conventional EHL theory. The contact is seen to be fully-flooded for all conditions tested. The widely-used thermal EHL correction of Gupta is shown to overcorrect for the film thickness reduction even at modest SRRs. Finally, the influence of the sliding direction on traction and film thickness is discussed for this set-up, and a thermal model is proposed to explain the observed behaviour.

Graphical abstract



Keywords EHL · Traction · Thermal effects in EHL · EHL film geometry

Extended author information available on the last page of the article

List of symbols

a	Hertz contact half-width $a = \left(\frac{3wR}{2E'}\right)^{\frac{1}{3}}$ [m]
B	Exponential parameter in VFT viscosity model [K]
Bi	Biot number [−]
c	Specific heat capacity [J/kgK]
D	Deborah number [−]
E_1, E_2	Ball (1) and Disc (2) elastic modulus [Pa]
E'	Reduced contact modulus $E' = 2\left(\frac{1-\nu_1^2}{E_1} + \frac{1-\nu_2^2}{E_2}\right)^{-1}$ [Pa]
F^+, F^-	Traction force in forward (+) and reverse (-) sliding [N]
F_0^+, F_0^-	Traction force under zero-sliding for $U_e = U_1$ (+) and $U_e = U_2$ (-) [N]
G_e	Equivalent shear modulus considering contact elasticity [Pa]
G_p	Fluid shear modulus in contact [Pa]
h	Coefficient of convective heat transfer [W/m^{2}K]
h_c	Central film thickness [m]
L_c	Characteristic length of thermal mass [m]
L_T	Gupta thermal loading parameter [−]
Na	Nahme-Griffith Number [−]
$\overline{p}$	Mean Hertz Pressure $\overline{p} = \frac{2}{3}P_0$ [Pa]
P_0	Maximum Hertz Pressure $P_0 = \left(\frac{3wE'^2}{2\pi^3R^2}\right)^{\frac{1}{3}}$ [Pa]
R	Ball radius [m]
SRR	Slide-Roll Ratio SRR $= \frac{U_s}{U_e}$ [%]
t_d	Characteristic timescale for heat diffusion [s]
t_r	Period of specimen rotation [s]
T_0	Temperature offset parameter in VFT viscosity model [K]
U_1, U_2	Ball (1) and Disc (2) surface velocity [m/s]
U_e	Entrainment speed $U_e = \frac{1}{2}(U_1 + U_2)$ [m/s]
U_s	Sliding speed $U_s = U_2 - U_1$ [m/s]
w	Normal contact load [N]
α	Pressure-viscosity coefficient (film-thickness-derived) [Pa^{-1}]
$\dot{\gamma}$	Nominal shear strain rate $\dot{\gamma} = \frac{U_s}{h_c}$ [s^{-1}]
η	Bulk fluid viscosity [Pa.s]
η_0	Scaling parameter in VFT model [Pa.s]
$\bar{\eta}_p$	Mean piezoviscous viscosity in contact [Pa.s]
κ	Thermal conductivity [W/mK]
μ	Traction coefficient [−]
μ_+, μ_-	Traction in forward (+) and reverse (−) sliding [−]
ρ	Density [kg/m^3]
$\bar{\tau}$	Mean shear stress $\bar{\tau} = \frac{\mu w}{\pi a^2}$ [Pa]
τ_e	Eyring stress [Pa]
χ	Thermal diffusivity $\chi = \frac{\kappa}{\rho c}$ [m^2/s]

1 Introduction

Elastohydrodynamic lubrication (EHL) has received much research attention during the last 80 years [1–3], leading to classical regression equations still widely used for predicting EHL film thickness [4] and their subsequent validation by experiments [5]. These predictions assume however that the temperature field is uniform throughout the contact, and so are not valid at high entrainment speeds where there is significant inlet shear heating. Several thermal correction factors derived from numerical calculations have been proposed [6], but these do not generalise well to different lubricant chemistries. Unlike film thickness, prediction of EHL friction remains very challenging due to the strong dependence on lubricant rheology at high pressure and shear strain rate. Friction is less well-studied at high speeds, and there are no simple closed-form correction factors as there are for film thickness.

One application which is currently experiencing rapid growth is electric vehicle technology. As a result, there is a pressing need to accurately predict efficiency and component life in high-speed gearing in electric vehicles [7], which must transmit very high torques at low speeds, and where entrainment speeds in gear and bearing contacts may exceed 20 m/s. The ability to accurately predict the influence of lubricant rheology on transmission efficiency is currently of great importance in the optimisation of this emerging technology [8]. The problem is compounded by the thermal coupling to macroscopic thermal resistances in these systems, the complexity of their geometries, and therefore the wide range of length-scales and time-scales involved. High-speed thermal EHL is also relevant to high-speed machine spindle bearings [9] and geared turbofan engines [10], but it is the need to simultaneously optimise both system energy efficiency and reliablity in electric vehicles that has brought thermal EHL traction losses more sharply into focus. This paper uses the term 'traction' to describe friction in the full-film EHL regime, to emphasise that the forces are transmitted via the fluid film, and not due to solid-solid interactions.

The pioneering EHL solution of Ertel [11, 12] assumed that film thickness and traction are largely decoupled. This is the case under conditions where the contact can be considered isothermal because the film thickness is governed by lubricant rheology in the inlet, in which the pressure and shear rate are low compared to the conditions in the contact itself. Film thickness is therefore well-predicted by low-shear lubricant properties measured at ambient pressure [13]. Traction however depends on the in-contact rheology, which is subject to sub-millisecond transit times, GPa pressures, and shear rates $\sim 10^7$ s^{-1}. The rheology of the fluid under these conditions is highly non-Newtonian and is still the subject of considerable debate [14, 15], in particular the

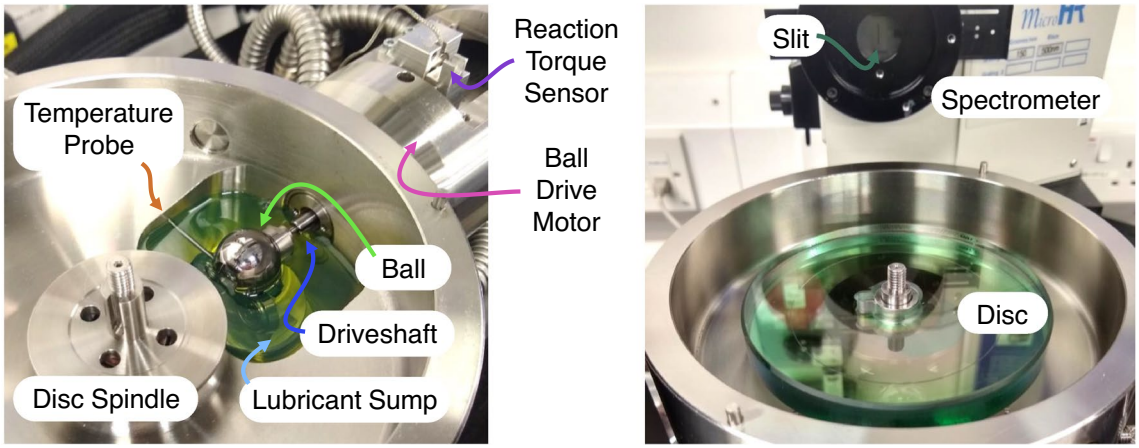


Fig. 1 EHD-HS test set-up showing driven steel ball resting on roller carriage, partially immersed in lubricant, with temperature probe positioned near to the contact outlet (left). The transparent disc (right) rests above the ball on the rotating disc spindle flange

Table 1 Material properties of contacting bodies

	Young's modulus E [GPa]	Poisson ratio ν [−]	Thermal conductivity κ [W/mK]	Thermal diffusivity χ [mm^2/s]
Sapphire	345	0.27	33	10.9
BK7 glass	75	0.22	1.1	0.52
AISI 52100 steel	210	0.3	21	6.1

treatment of the effect of high pressures and high shear rates. These effects are not well-resolved by EHL traction measurements due to the highly non-uniform temperature and pressure fields, a limitation of classical efforts to describe fluid behaviour in EHL contacts [16, 17]. High-pressure viscometers have so far been unable to simultaneously produce representative magnitudes of shear rate and transit time actually seen by EHL contacts, partly due to the very challenging problem of decoupling the influence of heat generation on the rheology from the rheology itself [18]. Nevertheless, the separate treatment of pressure and shear rate by models fitted to various rheology studies has resulted in several numerical solvers whose outputs show very good agreement with experiments [19, 20].

Fluid which is not entrained into the contact must be diverted around it, creating an inlet flow field with significant shearing, which generates heat. The heating becomes more significant as the entrainment speed increases. The consequent reduction in fluid viscosity in the inlet reduces film thickness at high entrainment speeds. So-called 'inlet shear heating' has been studied numerically by Cheng [21, 22], by Wilson and Sheu [23], and by Pandey and Ghosh [24], who provided expressions for central film thickness h_c of the form $h_{c_{\text{thermal}}} = h_{c_{\text{isothermal}}} C_T$, where C_T is a correction factor expressible as a function of fluid properties and contact conditions. The more recent, and widely-used, correction by

Table 2 Contact conditions using glass and sapphire discs under 50 N load

	Reduced modulus E' [GPa]	Max. hertz pressure P_0 [GPa]	Contact half-width a [μm]
Sapphire	284.9	1.3	137
BK7 glass	117.5	0.72	182

Gupta et al. [6] was appraised by the experimental study of Hili et al. [25] who used a high-speed ball-on-disc machine and ultra-thin-film interferometry [26]. Hili found qualitative agreement with Gupta's predictions, and provided alternative coefficients for four base oil types to better fit her measurements. Liang et al. [27] took a dual experimental and numerical approach, which they used to provide a unified set of modified coefficients for Gupta's correction and to investigate the influence of the temperature field on pressure profile and film shape.

In this work, simultaneous measurements of traction and film thickness are reported at entrainment speeds up to 20 m/s, using a high-speed optical tribometer developed during this study which implements a novel traction measurement technique. The extent to which the measurements deviate from the well-known EHL film thickness prediction of Chittenden, and the widely-used thermal correction of

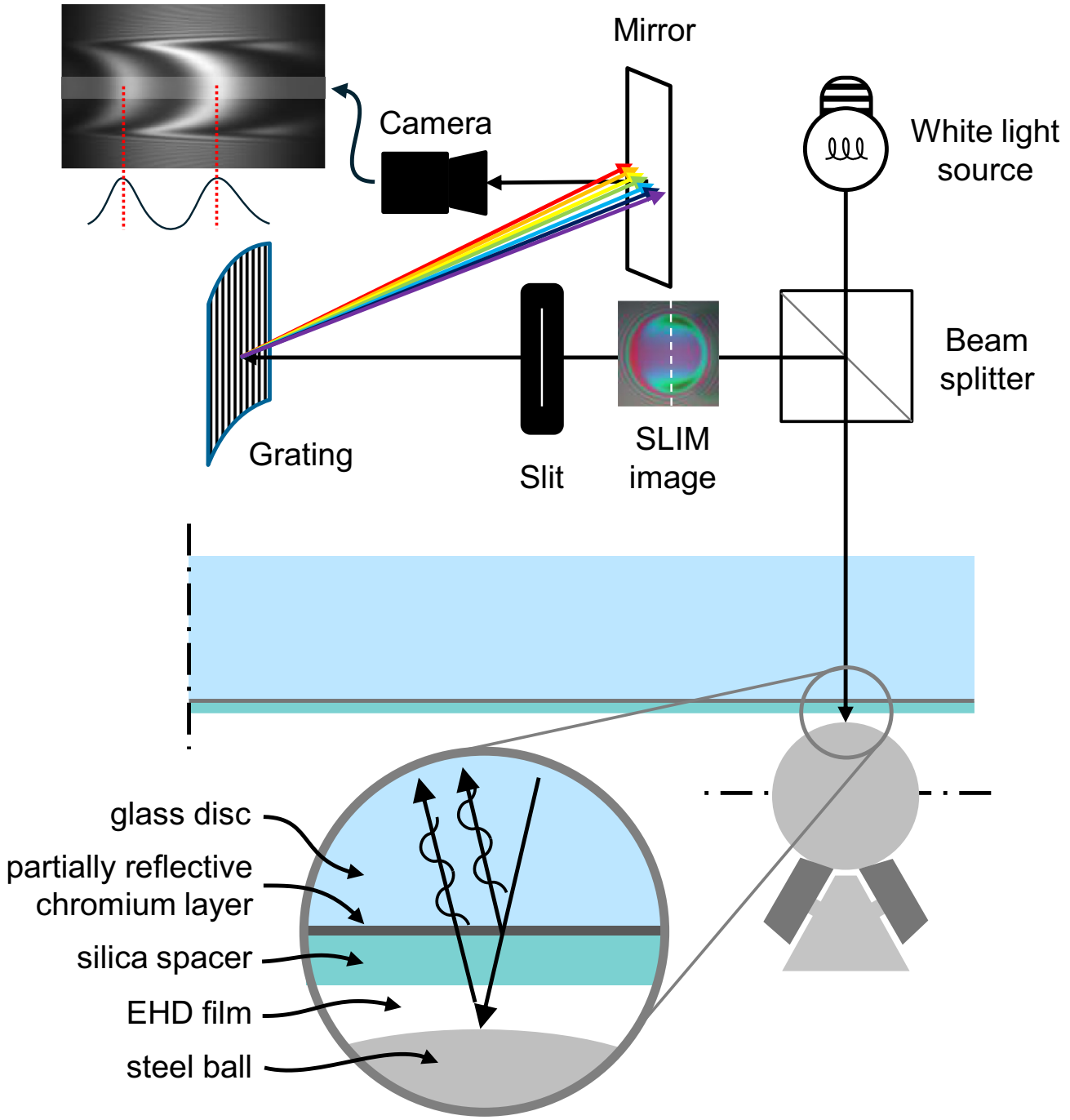


Fig. 2 Schematic of film thickness measurement by ultra-thin-film interferometry

Gupta, is quantified over a wide speed range for seven fluids chosen to represent base fluids commonly used in transmission lubricants. The traction measurements demonstrate the effect of fluid viscosity and chemical composition, showing the significant change in traction response with increasing entrainment speed. The implications of these measurements for understanding the thermal response of the contact, and the relevance of these findings to future efforts to measure traction at high speeds, particularly for dissimilar contacting materials, is discussed.

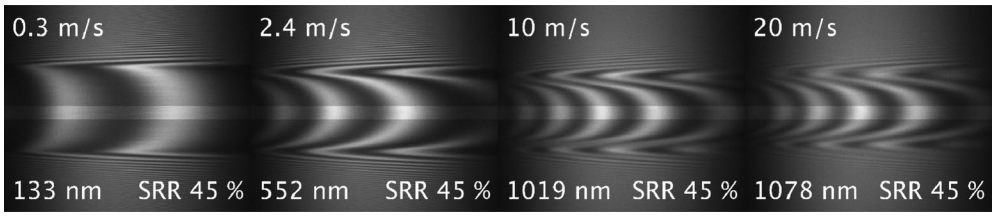


Fig. 3 Spectrograms taken with HVI 60 mineral oil for steel-on-glass contact at 45% SRR and 20°C, showing entrainment speeds and measured film thicknesses. The lighter band shows the position of the averaging region, from which the peaks used for the measurement of central film thickness are obtained

2 Methods

2.1 Test Set-up

A new test rig, the EHD-HS from PCS instruments, was used during this study. The machine comprises a rotating steel ball supported from below by three steel rollers, see Fig. 1, in contact with a transparent flat disc rotating directly above it, in the same manner as the EHD2 ultra-thin-film measurement system [26]. The ball and rollers are partially submerged in a temperature-controlled lubricant sump. The ball is loaded against the disc by the roller carriage, to which the load is transmitted via a load cell by a compliant lever connected to a lead-screw-type stepper motor, enabling load control. Ball and disc are mounted on separate perpendicular shafts driven independently by servomotors such that any surface speed between 0.05 and 20 m/s can be achieved on either surface, enabling independent control of entrainment and sliding speeds.

2.2 Contact Conditions

The ball specimens were made of standard AISI 52100 bearing steel, and discs made of both glass and sapphire were used. Specimen material properties are taken as those in Table 1. The balls were polished to a roughness below $R_a \approx 10$ nm, and the ball radius is 9.525 mm. The corresponding contact pressures are given in Table 2 for a ball load of 50 N.

2.3 Film Thickness Measurement

Film thickness measurements were made using ultra-thin-film interferometry [26], which is briefly described in this section. The transparent disc is coated on its contacting surface by a silica 'spacer layer', of thickness approximately 560 nm, and beneath that is a very thin semireflective chromium layer. White light is shone into the contact through the transparent disc, and is split by the chromium layer into a transmitted and a reflected beam, as shown in Fig. 2. When the surfaces are in motion, an elastohydrodynamic

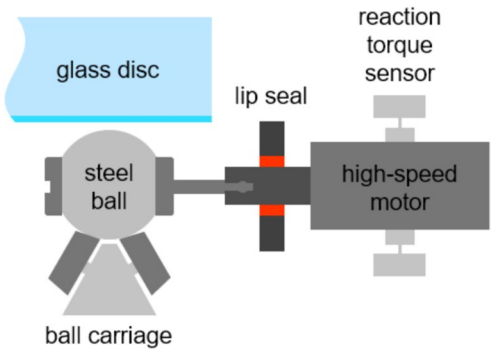


Fig. 4 Schematic of ball drive mechanism

lubricant film is developed between the ball and disc. The transmitted beam travels through the spacer layer and lubricant film, reflects off the ball, and recombines with the reflected beam at the chromium interface. The optical path difference between the two beams causes them to interfere destructively or constructively depending on wavelength. The resultant interferogram is then analysed using a spectrometer, which detects the wavelengths of minimum and maximum intensity, from which the optical path difference, and hence the film thickness, are calculated. At the start of each test, the spectrometer is used to measure the thickness of the spacer layer when the ball and disc are motionless and the film thickness is therefore zero. The spectrometer triggers at the same pre-specified angular position on the disc each time to ensure the spacer layer thickness is consistent for each measurement.

To enable EHL film and traction measurements at high speeds, the EHD-HS rig used in this study includes several modifications compared to previous implementations of this technique on standard EHD rigs. The ball-carriage rollers (which in previous setups comprise the cylindrical outer race of a centrally-mounted bearing) are conical, their cone angle being chosen to amortise spin in the contacts with the ball, thereby reducing parasitic carriage traction. The drive motors used are capable of achieving surface speeds of 24.5 m/s, and a camera exposure time of 1 ms is used to limit motion blur. A telecentric objective of magnification

5X, achieving a working distance of over 60 mm, enables sufficient separation between lubricant and lens to avoid oil splashing onto the lens, a much greater issue at high speeds due to flow turbulence. Example spectrograms are given in Fig. 3 to illustrate that these measures achieve adequate fringe visibility over the whole speed range.

Film measurements are performed from the analysis of five consecutive spectrometer measurements taken in quick succession (spaced by approx. 200 ms, or consecutive disc rotations, whichever is slower), so that the measurement is minimally affected by temperature transience. The temperature control of the lubricant is achieved by circulating silicon oil via a cooler through separate cooling channels in the steel pot, which also houses electrical resistance heaters, with the controller tuned to respond to rapid changes in energy dissipated by viscous shear, as the motor speeds change during the test. The temperature is measured approx. 5 mm from the outlet of the contact by a platinum resistance thermometer as in other setups. Temperature control of the oil reservoir to within ±1°C is achieved below 10 m/s. At higher entrainment speeds for some of the fluids tested, excursions from the nominal temperature greater than this were unavoidable, and the film thickness measurements have been corrected accordingly so as to be comparable at the nominal temperature, as detailed in Appendix A.

2.4 Traction Measurement

The EHD ultra-thin-film measurement system, although an inline torque sensor is included between the ball drive shaft and ball motor, cannot measure traction in the same way as other ball-on-disc tribometers designed for this purpose, such as the MTM. This is because the ball torque due to the ball-on-disc contact traction is superposed with the parasitic torques from the three ball-carriage bearings, fluid drag, and the radial lip seal on the driveshaft where it enters the sump (Fig. 4). These three additional torques are challenging to measure or estimate, and depend on the ball speed, temperature, load, and lubricant properties. In most cases they are of similar magnitude to the traction torque, thereby completely obscuring the measurement.

This study overcomes this problem by using a novel traction measurement procedure which enables these parasitic torques to be measured and eliminated. The technique relies on the assumption that the parasitic torques, although they depend on ball speed, are insensitive to disc speed. This assumption is weakest with reference to fluid drag, because the flow field depends on both surface speeds, but as the ball is only partially submerged in lubricant and the disc sits entirely above the fluid level, fluid drag is expected to be the smallest of the parasitic torques, and the influence of disc speed due to oil and air interactions is expected to be relatively weak.

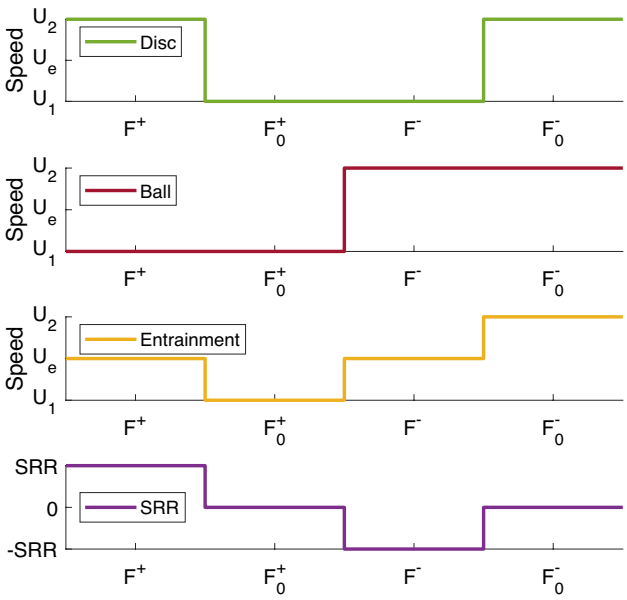


Fig. 5 Summary of ball and disc speeds under four cases used for traction measurement

Consider the case where an entrainment speed U_e and slide-roll ratio SRR (Eq. 1) are specified, and traction force under these conditions is to be measured. The meridional ball surface speed U_1 and disc tangential speed U_2 are given by Eq. 2, where a positive SRR implies the disc speed is greater.

$$\mathrm{SRR} = \frac{U_s}{U_e} = 2\frac{U_2 - U_1}{U_1 + U_2} \tag{1}$$

$$U_1 = U_e\left(1 - \frac{\mathrm{SRR}}{2}\right) \qquad U_2 = U_e\left(1 + \frac{\mathrm{SRR}}{2}\right) \tag{2}$$

If it is assumed that the traction forces due to positive and negative SRR are equal and opposite, then the sign of the nominal SRR is irrelevant for traction measurement; only the magnitude is significant (an assumption later discussed in the context of thermal EHL at high speeds). In this case, transducer offset can be removed by calculating the traction coefficient from Eq. 3 where traction force is denoted F, with a superscript indicating the sign of the sliding speed, such that F^+ and F^- have equal entrainment speed and opposite sliding direction, and w is contact load. This approach is relied upon in many widely-used tribometers including the MTM. It assumes that the only force contributing to F that changes with ball and disc speeds, arises from contact traction.

Table 3 Lubricants tested, showing measured kinematic viscosities and pressure-viscosity coefficients fitted from film thickness measurements

	Group	$\nu_{40°C}$ [cSt]	$\nu_{100°C}$ [cSt]	$\alpha_{20°C}$ [GPa^{-1}]	$\alpha_{60°C}$ [GPa^{-1}]	$\alpha_{100°C}$ [GPa^{-1}]
Heavy mineral oil	I	68.5	8.8	24.3	16.6	15.4
HVI 60	I	23.3	4.5	21.1	18.8	13.8
CHN 100R	II	21.2	4.4	21.1	16.5	13.6
Yubase 4	III	19.5	4.3	16.3	12.3	11.4
Spectrasyn 4 (PAO4)	IV	18.8	4.3	17.6	13.3	11.4
Durasyn 145 (PAO5)	IV	25.3	5.3	17.8	15.2	12.3
Santotrac 50	–	28.3	5.2	33.3	20.0	13.9

$$\mu = \frac{F^+ - F^-}{2w} \tag{3}$$

The EHD by contrast sees several forces contributing to F which all depend on ball speed, and cannot therefore use the difference between F^+ and F^- to measure traction if the ball speed is different for the F^+ and F^- measurements. One approach to overcome this, used by the EHD2, is to set the ball speed equal to the nominal entrainment speed in both cases, and to enforce the sliding by changing only the disc speed. This is undesirable as the F^+ and F^- cases have different entrainment speeds and hence any nonlinearity in the traction response (such as that introduced by thermal effects) influences the measurement and is not itself quantifiable.

The novel method proposed here addresses this issue. An additional two new measurements of traction force are introduced, in which the SRR is zero, and so (close to) zero traction force is expected. In the F_0^+ case, the disc speed is brought to the same speed as the ball when F^+ was measured, and likewise F_0^- implies both surfaces match the ball speed used for F^- measurement. F_0^+ and F_0^- therefore measure the ball parasitic torques when the ball speed is equal to U_1 and U_2, respectively. The traction coefficient in each sliding direction can therefore be calculated from Eq. 4. The assumption that forward and reverse-sliding traction are equal and opposite leads to Eq. 5.

$$\mu_+ = \frac{F^+ - F_0^+}{w} \qquad \mu_- = -\frac{F^- - F_0^-}{w} \tag{4}$$

$$\mu_{\text{avg}} = \frac{\mu_+ + \mu_-}{2} = \frac{\left(F^+ - F_0^+\right) - \left(F^- - F_0^-\right)}{2w} \tag{5}$$

The $(F^+ - F_0^+)$ term represents forward traction force, and the $(F^- - F_0^-)$ term reverse traction force. The four traction measurements are taken in the sequence shown in Fig. 5 by a series of 10 ms bursts from the transducer, accumulated after the motor speeds have stabilised until a stable average traction force is obtained over 10 consecutive bursts (total range within ±0.032 N) or until 2 s have elapsed.

2.5 Lubricants

Seven different lubricants were used in this study, chosen to cover a range of base oil types and a viscosities. These are listed in Table 3 together with their kinematic viscosities. Table 3 also lists estimated pressure-viscosity coefficients for each fluid; these are derived from film thickness measurements and should not therefore be interpreted as describing lubricant rheology. The film thickness prediction according to Chittenden [28] for circular contact is fitted by finding the best fit line with gradient 0.68 on the plot of log (h_c) vs log (U_e) for $U_e \leq 2.4$ m/s and SRR ≤ 4%. All other parameters are known *a priori*, such that, once h_c is measured, α can be calculated.

Dynamic viscosity and density were measured at a low shear rate (below 10^3 s^{-1}) at atmospheric pressure for each fluid using a Stabinger SVM 3000 viscometer, at a series of 5 temperatures between 20°C and 100°C. Refractive index

Table 4 Regression parameters used to calculate viscosity, density and refractive index for lubricants tested, as per Eqs. 6, 8 and 9

	η_0 [mPa.s]	B [K]	T_0 [K]	ρ_1 [kg/m^3°C]	ρ_0 [kg/m^3]	n_1 [°C^{-1}]	n_0 [−]
Mineral oil	0.04901	1007.7	170.9	−0.6125	874.6	−0.000363	1.482
HVI 60	0.06948	797.4	172.2	−0.6315	875.5	−0.000342	1.485
CHN 100R	0.07021	803.7	167.6	−0.6285	852.3	−0.000315	1.471
Yubase 4	0.06970	807.7	164.6	−0.6310	844.0	−0.000339	1.469
Spectrasyn 4	0.06576	843.3	158.1	−0.6275	829.3	−0.000339	1.466
Durasyn 145	0.05365	951.7	153.0	−0.6235	833.4	−0.000339	1.466
Santotrac 50	0.1330	630.2	193.0	−0.6450	913.7	−0.000334	1.495

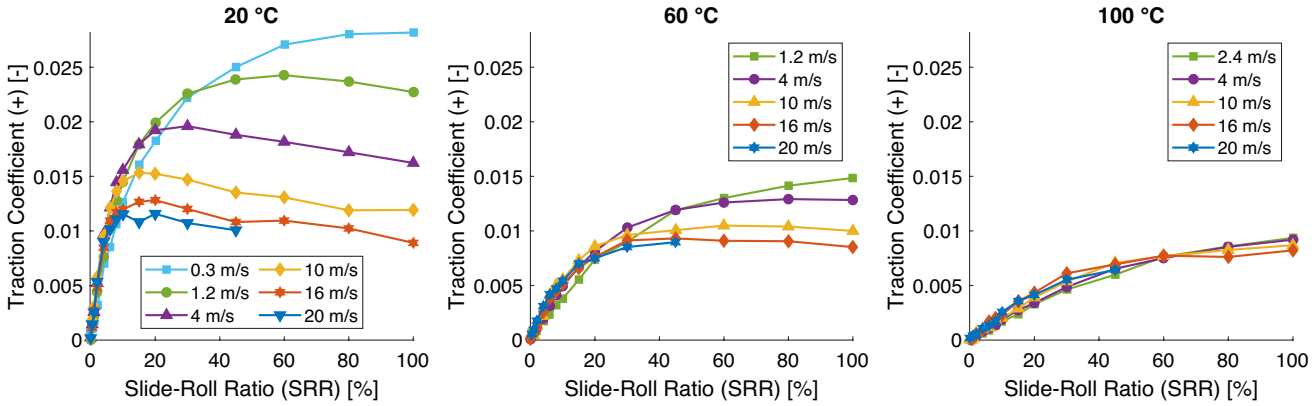


Fig. 6 Traction curves measured for PAO4 at three temperatures for selected entrainment speeds in forward sliding, disc faster

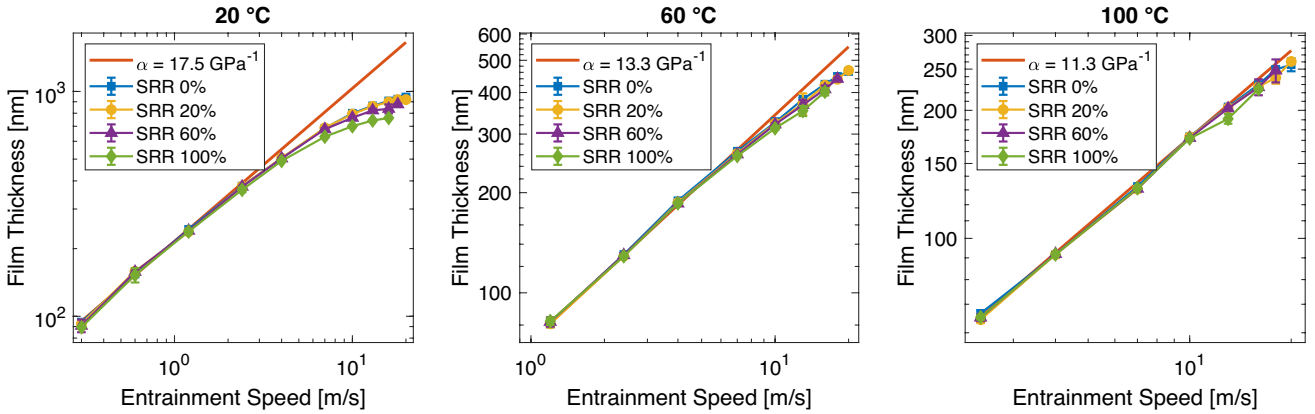


Fig. 7 EHD central film thickness vs entrainment speed measured for PAO4 at three temperatures for selected SRRs in forward sliding. Each film thickness shown is the mean of 5 consecutive measurements with error bars located at $\pm 3\sigma$. The film thickness prediction of Chittenden, obeying the relationship $h_c \propto U_e^{0.68}$ is also shown, where the pressure-viscosity coefficient α given in the legend is the only unknown and so has been fitted from low-speed film thickness measurements ($U_e \leq 2.4$ m/s)

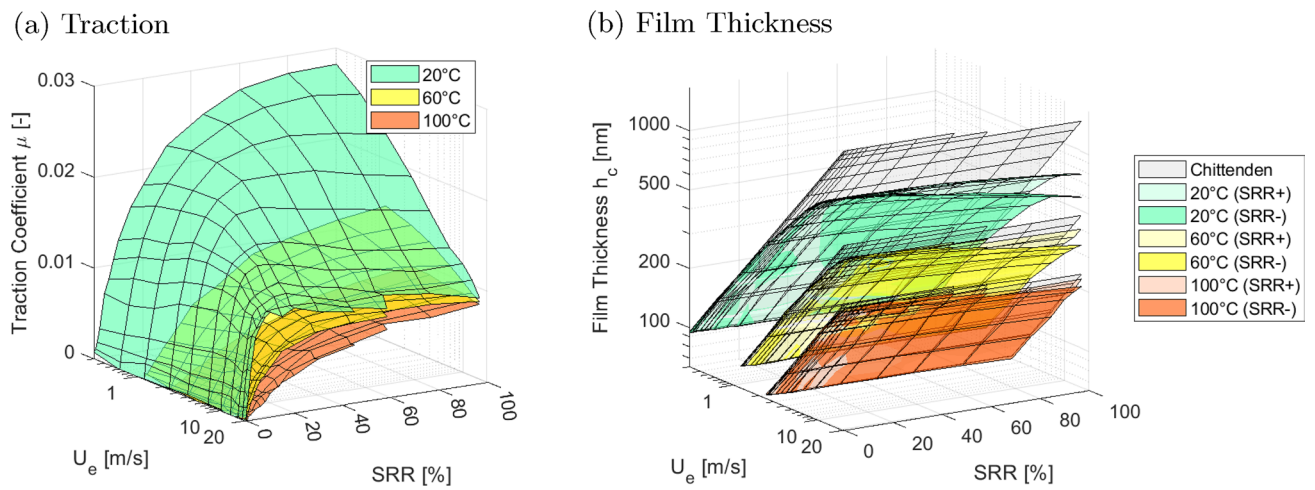


Fig. 8 Traction and film thickness vs entrainment speed U_e and slide-roll ratio SRR measured simultaneously for three temperatures with PAO4

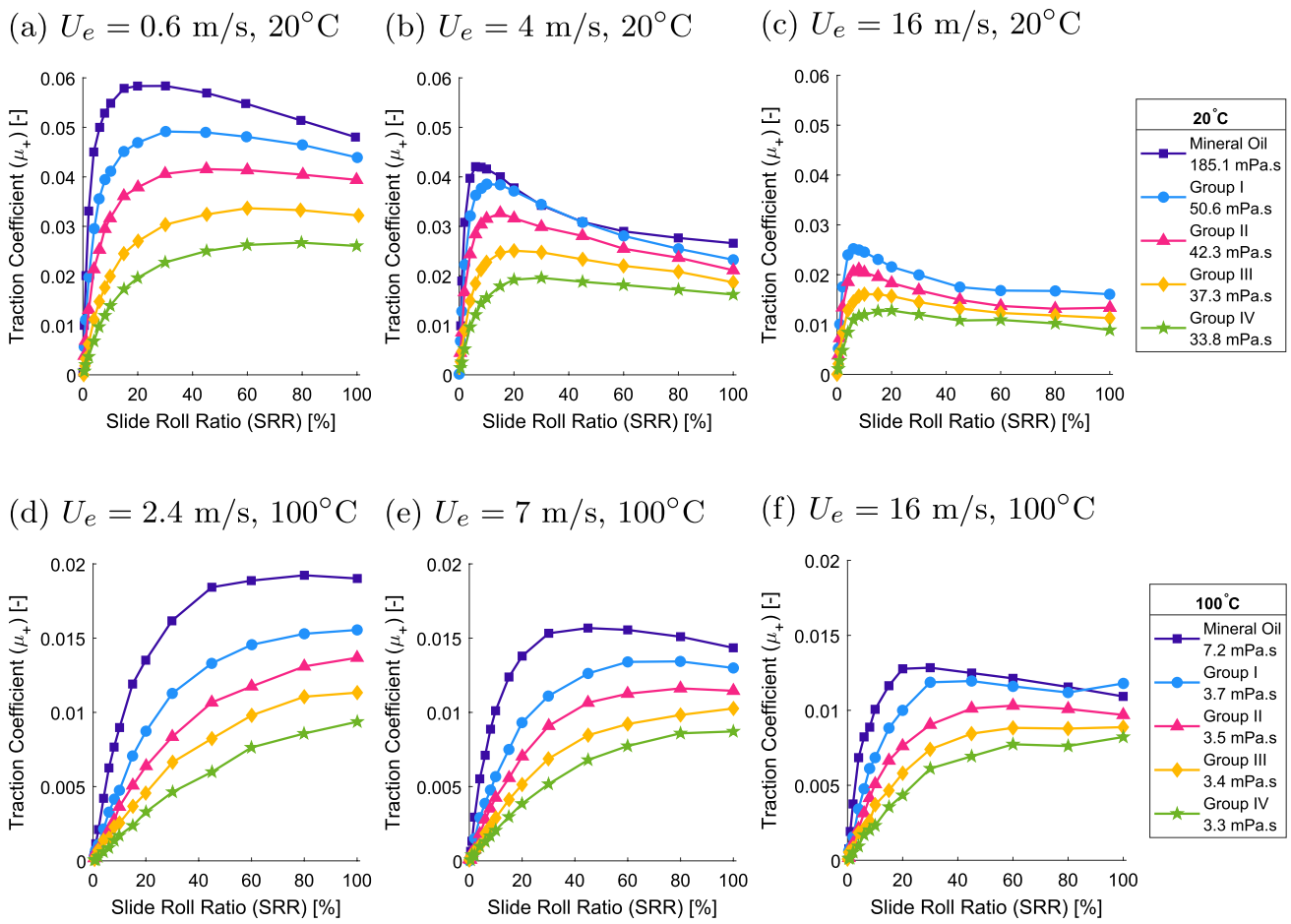


Fig. 9 Traction curves for various speeds at 20°C (**a**, **b**, **c**) and 100°C (**d**, **e**, **f**), for five fluid types spanning Groups I–IV, with corresponding dynamic viscosities given in the legend for each. Steel ball on glass disc, 50 N load, 0.73 GPa max. Hertz pressure

was measured at the sodium D-lines at $\{40, 60, 80, 90\}$°C using an Abbe refractometer. The Vogel–Fulcher–Tammann (VFT) viscosity model [29] (Eq. 6), was fitted to the viscosity-temperature data, incurring errors smaller than ±0.5% in all cases.

$$\eta = \eta_0 e^{\frac{B}{T-T_0}} \tag{6}$$

The parameters $\ln(\eta_0)$, T_0 and $B - T_0 \ln(\eta_0)$ were obtained by multivariate linear regression from Eq. 7, which follows from Eq. 6 and is of form $y = a_1 x_1 + a_2 x_2 + k$, to give η_0, T_0 and B.

$$T \ln \eta = T \ln \eta_0 + T_0 \ln \eta + B - T_0 \ln \eta_0 \tag{7}$$

Linear dependence of density ρ (Eq. 8) and refractive index n (Eq. 9) with temperature is assumed. The linear models were found to incur errors not exceeding ±0.1% compared to measurements.

$$\rho = \rho_1 T + \rho_0 \tag{8}$$

$$n = n_1 T + n_0 \tag{9}$$

The parameters obtained by these regressions are given in Table 4, assuming T in Kelvin for viscosity, and T in °C for density and refractive index. Dynamic viscosity η is given in mPa · s and density in kg/m^3.

2.6 Test Procedure

Traction coefficient and film thickness were measured simultaneously for entrainment speeds in the set

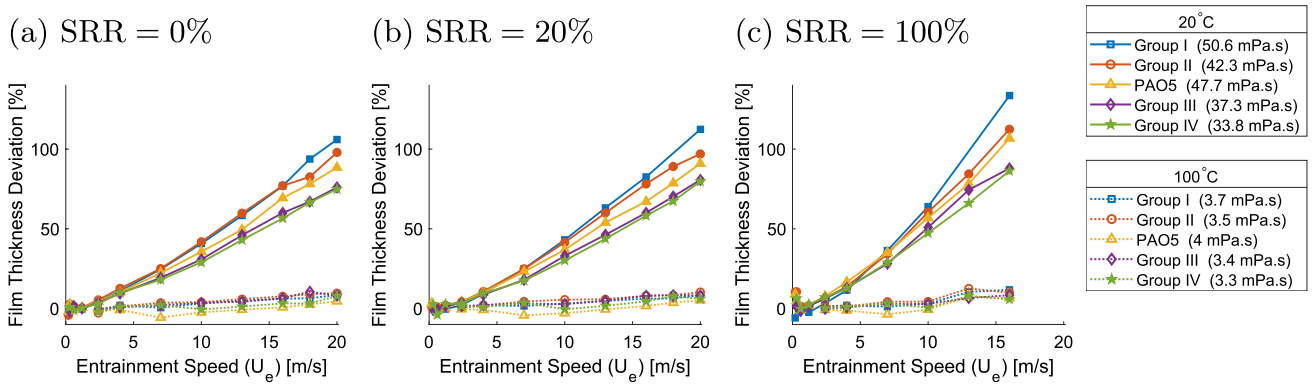


Fig. 10 Percentage overestimation, compared to measurement in positive sliding direction, of central film thickness h_c from the Chittenden model at 20°C and 100°C for three SRRs, with corresponding dynamic viscosities shown in legend

$\{0.05, 0.1, 0.2, 0.3, 0.6, 1.2, 2.4, 4, 7, 10, 13, 16, 18, 20\}$ m/s, and for slide-roll ratios in the set $\{0, 0.5, 1, 2, 4, 6, 8, 10, 15, 20, 30, 45, 60, 80, 100\}$ %, producing, for each test, a series of film thickness and traction measurements. These were performed at temperatures 20, 60, 100°C. In total, over 6500 film thickness and traction measurements were made. Measurements were taken only for conditions where:

- The minimum predicted film thickness $h_{\min}$ according to Chittenden [28] exceeded 40 nm, guaranteeing a Λ ratio greater than 3, and hence maintaining full-film conditions.
- The central film thickness measured was less than 2 µm, above which the resolution of the ultra-thin-film interferometry technique begins to degrade significantly.
- The specimen speeds were strictly slower than 24.5 m/s (hence the highest SRR tested at 20 m/s entrainment was 45 %).

3 Results

3.1 Measurements of Traction and Film Thickness

Example traction coefficients (μ^+, positive SRR, disc faster) for PAO4 (polyalphaolefin) are shown in Fig. 6 for a selection of entrainment speeds. The simultaneously-measured central film thicknesses are shown in Fig. 7.

These data are summarised by the 3D plots in Fig. 8, which show the traction (Fig. 8a) and film thickness (Fig. 8b) measurements vs both U_e and SRR. Similar plots were obtained for each fluid, over 400 simultaneous traction and film thickness measurements having been conducted for each, and these are included for reference as Supplementary Data.

Traction curves for four base fluid types (Group I is represented twice at two different viscosities) are shown in Fig. 9, which demonstrates that the novel traction measurement method successfully replicates familiar trends and

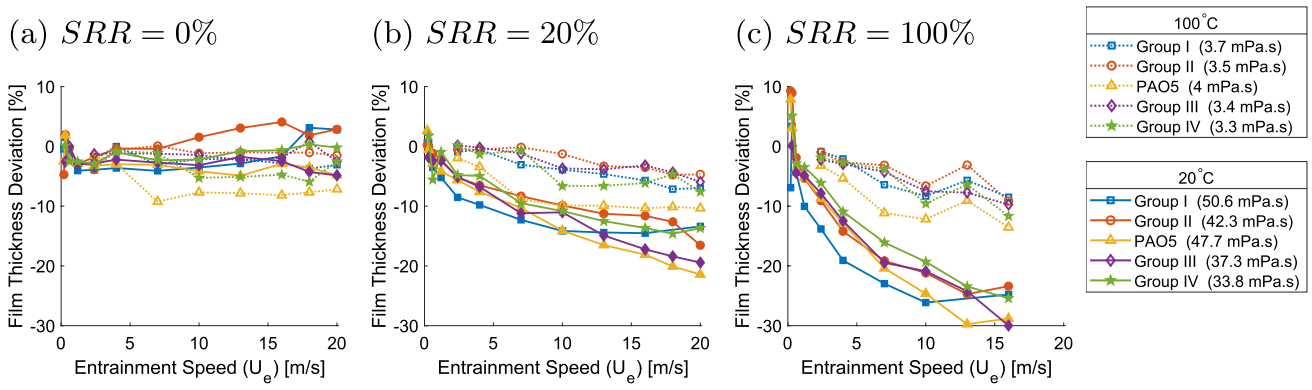


Fig. 11 Percentage difference between central film thickness h_c predicted by Gupta model, and measurement in positive sliding direction, for 20°C and 100°C with corresponding dynamic viscosities shown in legend

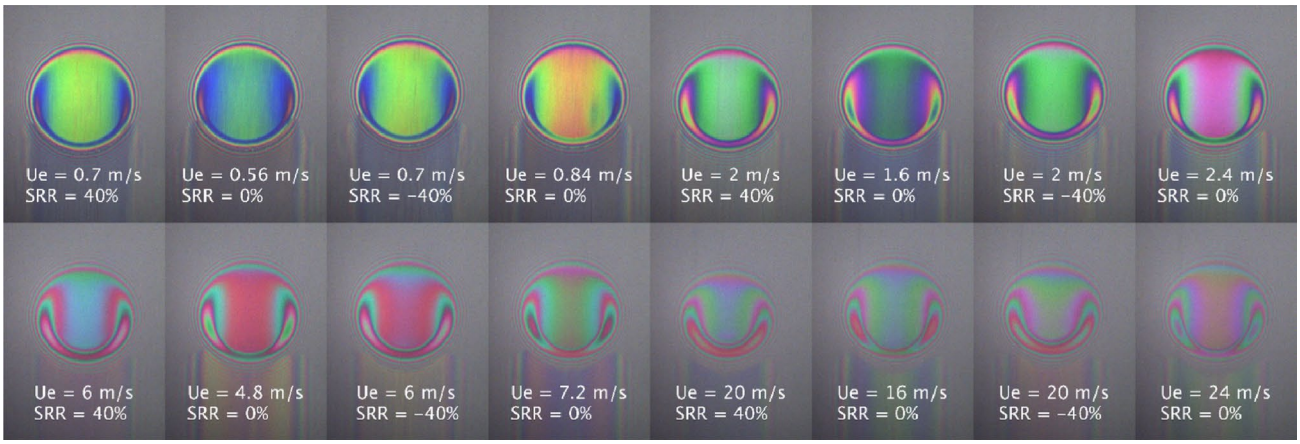


Fig. 12 Interferometric images of ball-on-disc contact for steel-on-glass, 50N (0.73 GPa), 20°C for PAO5 at four nominal entrainment speeds and 40% SRR, showing each of the four measurements from Fig. 5 in the sequence they were measured

representative values of EHD friction for these base fluids at various speeds and temperatures. The four lowest-viscosity fluids are chosen to have comparable viscosity at 100°C, although their different viscosity indices lead to differing viscosity at lower temperatures.

It can clearly be seen in Figs. 7 and 8b that film thickness is lower than the corresponding Chittenden prediction [28] at high speeds. The reduction is the greatest at lower temperatures, high slide-roll ratios, and in the negative sliding direction. At higher speeds the traction curve has larger gradient at low slide-roll ratios, and flatter gradient above the maximum-traction point. Film thickness continues to depend comparatively weakly on SRR even beyond the maximum-traction point, until approx. 50% SRR when there is a slight reduction for forward sliding, and a more pronounced reduction for negative sliding. The contact remains fully-flooded, and the reduction in film thickness at high speeds is not due to inlet starvation, as shown in Fig. 12 later.

3.2 Comparison to Film Thickness Predictions

The deviation from the film thickness predicted by Chittenden is quantified in Fig. 10. The film thickness deviation is given as a percentage of the measurement in forward sliding, according to Eq. 10. It is evident that the predicted film thickness can exceed the measured thickness by a factor of as much as 2 in pure rolling at 20 m/s. The overprediction is the largest at 20°C for the 4 cSt fluids. This effect depends on both base fluid type (Group I and II oils show greater deviation) and base fluid viscosity (compare PAO5 to PAO4, labelled 'Group IV', higher viscosity increases the deviation). At 100°C, and hence for low viscosities of the order 4 mPa.s however, the difference between measured and predicted film thicknesses is very small.

$$\delta h_c = \frac{h_{\text{Chittenden}} - h_c^+}{h_c^+} \times 100\% \tag{10}$$

Film thickness measurements are also compared in the same way to the model of Gupta, (Eqs. 11 and 12), where L_T is the thermal loading parameter, P_0 is the maximum Hertz pressure, and κ_{oil} is the thermal conductivity of the fluid, taken here as a first approximation to be 0.15 W/mK.

$$h_{\text{Gupta}} = \frac{h_{\text{Chittenden}}\left(1 - 13.2\frac{P_0}{E'}L_T^{0.42}\right)}{1 + 0.213\left(1 + 2.23\text{SRR}^{0.83}\right)L_T^{0.64}} \tag{11}$$

$$L_T = -\left(\frac{\partial \eta}{\partial T}\right)\frac{U_e^2}{\kappa_{\text{oil}}} = \frac{\eta B}{\left(T - T_0\right)^2}\frac{U_e^2}{\kappa_{\text{oil}}} \tag{12}$$

The gradient of viscosity with temperature in Eq. 12 is calculated analytically from Eq. 6 using the relevant parameters from Table 4. The deviations of the current measurements for the Gupta predictions obtained in this way are plotted in Fig. 11, which shows that the Gupta model under-predicts the measurement by around 25% at 100% SRR in rolling-sliding conditions. However, the Gupta model is quite accurate in pure rolling, incurring errors not more than 10% for the fluids and conditions tested here.

3.3 Interferometric Images of the Contact

An additional test was conducted with PAO5 at 20°C, using an LED white light source and an RGB camera to record the interferogram of the whole contact directly, instead of using

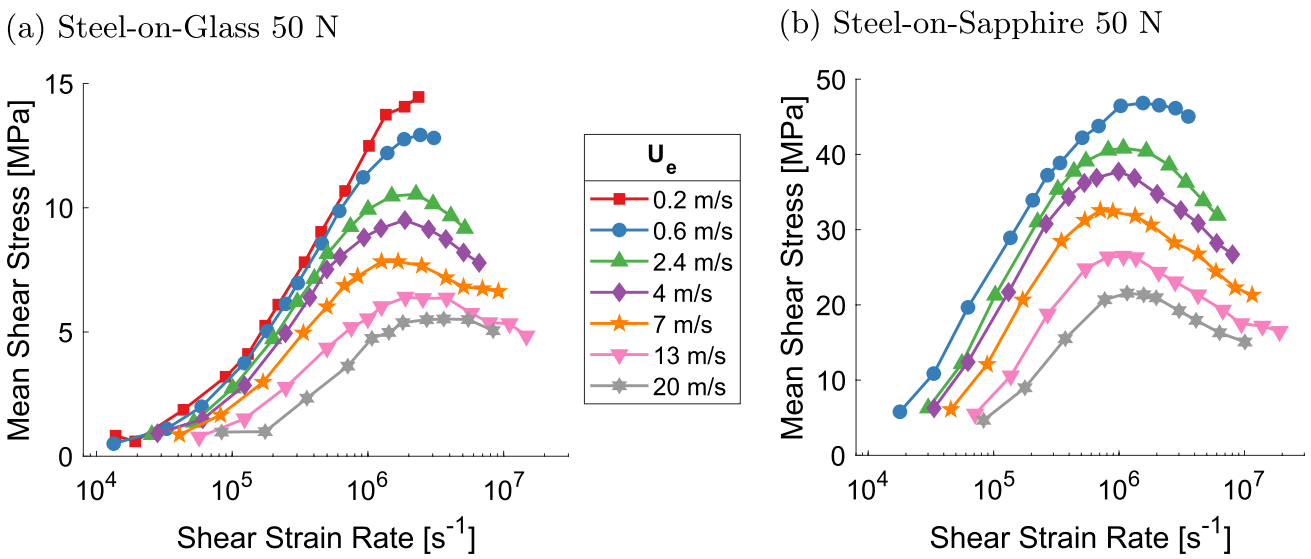


Fig. 13 Mean shear stress $\bar{\tau}$ vs shear strain $\dot{\gamma}$ for PAO5 (Group IV) with a steel ball on glass disc (**a**) and sapphire disc (**b**) at 20°C and 50 N load for selected speeds (forward sliding, disc faster)

the spectrometer. Interferometric images of the contact at selected speeds are shown in Fig. 12. These provide some insight in to EHL film shape at different entrainment and sliding speeds and confirm that:

- At all entrainment speeds up to 24 m/s, the characteristic features of an EHD contact are retained, namely a wide central plateau, a sharp constriction at the outlet, and regions of minimum film thickness on the sidelobes.
- The contact remains fully-flooded, there is no starvation and no transition in behaviour of the cavitation region up to 24 m/s entrainment in this set-up. This confirms that any reduction in film thickness observed at high speeds is not due to inlet starvation.
- The central plateau remains wide enough, and the image stable enough even at the highest speeds employed here (24 m/s), to reliably measure central film thickness.
- No central dimple was observed (this is true of all tests in this study).
- The shape of the outlet region changes under high-sliding conditions (SRR>10%) at high speeds, with the sidelobes coalescing as the outlet constriction expands in the entrainment direction, consistent with the findings of Hili [25] and Liang [27].

3.4 Mean Shear Stress and Shear Strain Rate

Simultaneous measurements of both traction and film thickness enable the calculation of both mean shear stress $\bar{\tau}$ (Eq. 13) and shear strain rate $\dot{\gamma}$ (Eq. 14).

$$\bar{\tau} = \frac{\mu w}{\pi a^2} = \mu \bar{p} \tag{13}$$

$$\dot{\gamma} = \frac{U_s}{h_c} \tag{14}$$

The true shear stress and shear strain rate experienced by the fluid are non-uniform throughout the contact, and highly spatially nonlinear. The mean values calculated here are therefore not intended to describe fluid rheology, but are convenient normalisations of traction and film thickness which allow comparisons between fluids and contact conditions, and which illustrate the change in traction response at high speeds. Mean shear stress vs strain rate is shown for a PAO5 in a steel-on-glass contact in Fig. 13a, and for steel-on-sapphire in Fig. 13b. Note that the strain rate ranges compare well between figures because the film thicknesses measured were similar, the dependence of reduced contact modulus in regression equations for film thickness being relatively weak ($h_c \propto E'^{-0.117}$).

These figures contain five features worthy of note:

1. At low shear strain rates a Newtonian/viscoelastic behaviour is seen as an increasing gradient on the linear/log graph.
2. At high strain rates, shear stress is considerably reduced as a result of the thermal response of the film to shear heating, which reduces mean viscosity in-contact. This reduction eventually becomes so severe that the gradient of shear stress with strain rate becomes negative.
3. At intermediate strain rates there is a region of shear-thinning behaviour which appears to obey the Eyring

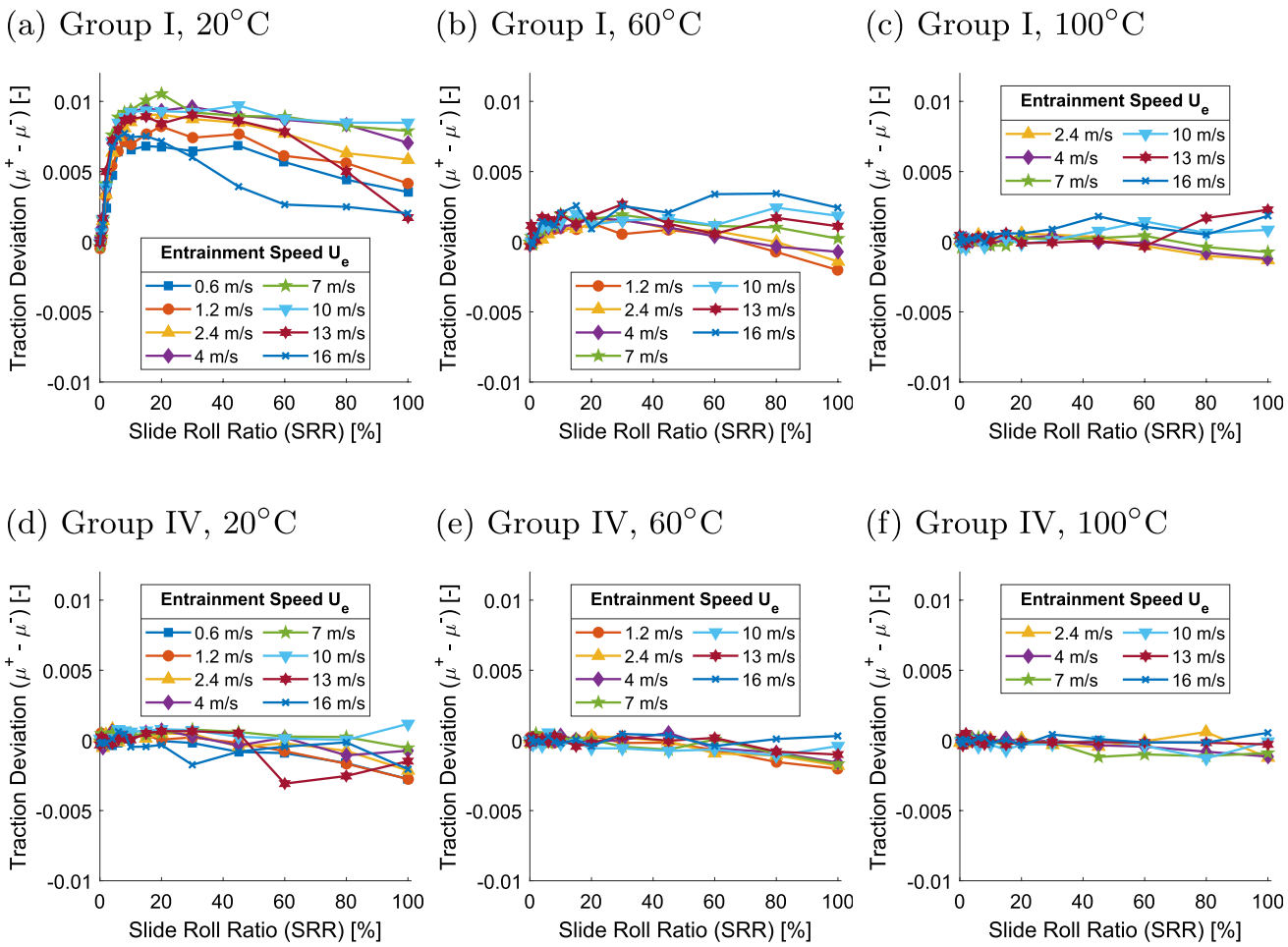


Fig. 14 Difference between traction coefficient in forward and reverse sliding directions for Group I (**a**, **b**, **c**) and Group IV (**d**, **e**, **f**) fluids of similar ν_{100}, vs SRR for selected entrainment speeds. Traction difference is confined to within the noise threshold of ±0.002 for PAO5 in the steel-on-glass contact at all three temperatures, but for the Group I fluid at the lowest temperature the average traction metric incurs errors ∼ ±0.005

model, clearly seen here as a proportionality between $\bar{\tau}$ and $\log(\dot{\gamma})$. The origins, applications and limitations of the Eyring model are discussed in great detail by Spikes and Zhang [14].

4. At high entrainment speeds, the shear stress is lower than at low speeds, for equivalent shear rate. This effect is evident even at speeds below which there is significant reduction in film thickness, and at shear rates well below the bounds of the thermoviscous regime. Spikes and Zhang [14] note that the viscoelastic term is significant when contact transit times are short (less than $\sim 10^{-4}$ s) and shear rates are low (less than 10^5 s^{-1}). At $U_e = 20$ m/s, transit times are of the order 10^{-5} s, so we may consider the shortening of transit times at high entrainment speeds to extend the significance of the reduction in shear stress by viscoelasticity to higher shear rates.
5. The gradient of the linear regime (which corresponds to the Eyring stress τ_e) decreases at very high speeds, the onset of this decrease corresponding to the speeds at which the film thickness falls significantly below Chittenden's prediction.

3.5 Changes in Traction and Film Thickness with Sliding Direction

It was found during the development of the method that both traction and film thickness varied in a repeatable manner between forward (disc faster) and reverse (ball faster) sliding direction. The difference between the traction coefficients measured in forward and reverse sliding is shown in Fig. 14 for two fluids and three temperatures. The magnitude of the traction difference varied with fluid viscosity, fluid type, and contact pressure, and was found only to be significant for fluids, viscosities and contact conditions leading to mean shear stresses greater than 4.0 MPa. Figure 14 shows that the μ^+ and μ^- cases are significantly different at 20°C for the Group

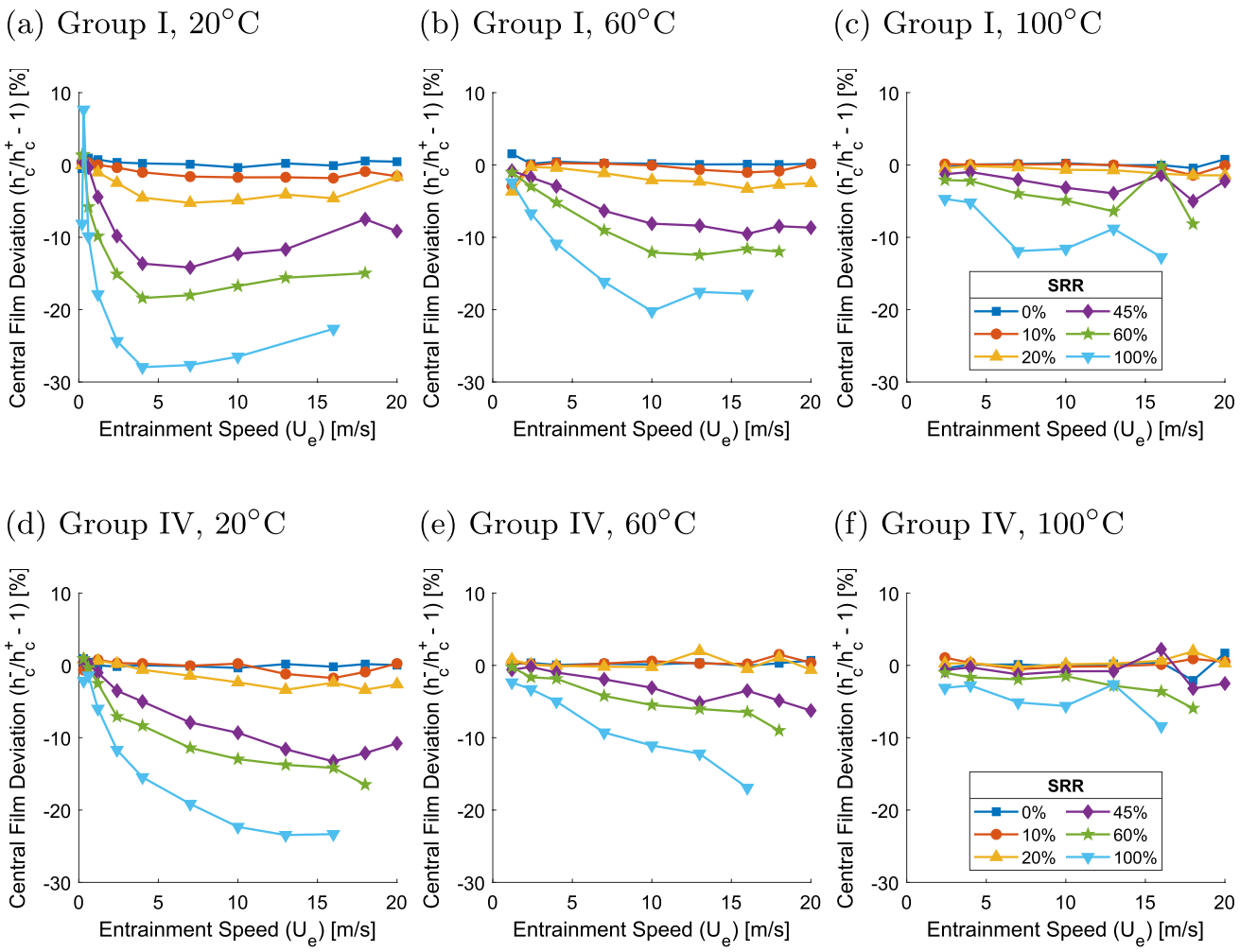


Fig. 15 Percentage difference between central film thickness h_c in forward and reverse sliding directions for Group I (**a**, **b**, **c**) and Group IV (**d**, **e**, **f**) fluids of similar v_{100}, vs entrainment speed for selected SRRs

I fluid, but that this effect is not seen at the same temperature (and similar viscosity) for the Group IV fluid (at the lower contact pressure). This suggests that the effect originates from the rheology of the fluid in-contact, and not from the higher far-field fluid viscosity incurring a speed-dependent drag on the ball specimen and hence influencing the traction measurement. This demonstrates the validity of the assumption that the difference in drag due to oil flow around the ball between the forward and reverse sliding cases is negligible. In circumstances where the specimens in contact have different material properties, geometries and/or contact track lengths, it is therefore necessary to measure traction and film thickness in the forward and reverse cases separately, or at least to state the sliding direction. The definition in Eq. 5 should be avoided unless it can be shown not to differ from the unidirectional case for all conditions tested.

The difference in central film thickness between forward and reverse sliding conditions is shown for a Group I and a Group IV fluid, each at three temperatures, in Fig. 15. This difference depends strongly on viscosity, and weakly on base fluid type at low speeds. It was only found to be significant at relatively high SRRs (>20%), and lower temperatures (higher viscosities, above ~20 mPa.s) produce a more pronounced difference. At low speeds, the difference increases with entrainment speed. It appears from Fig. 15a that at 20°C there is an entrainment speed above which the effect diminishes in magnitude, approx. 4 m/s for the Group I fluid. From Fig. 15d this speed appears closer to 16 m/s for the Group IV fluid. Thus it seems that this speed depends on base fluid type (although the evident viscosity contribution may also be significant given these two fluids do not have the same viscosity at 20°C).

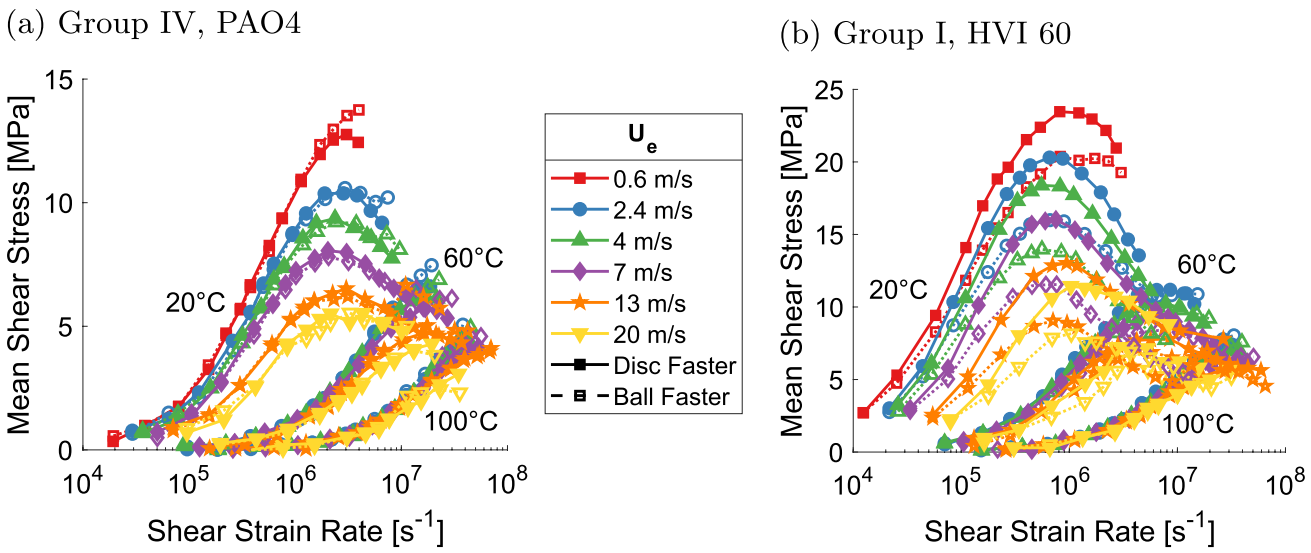


Fig. 16 Mean shear stress $\bar{\tau}$ vs shear strain rate $\dot{\gamma}$ for base fluids in Group IV (**a**) and Group I (**b**) at three temperatures, steel ball on glass disc at 50 N load for selected speeds, showing the effect of base fluid type on shear stress under forward and reverse sliding

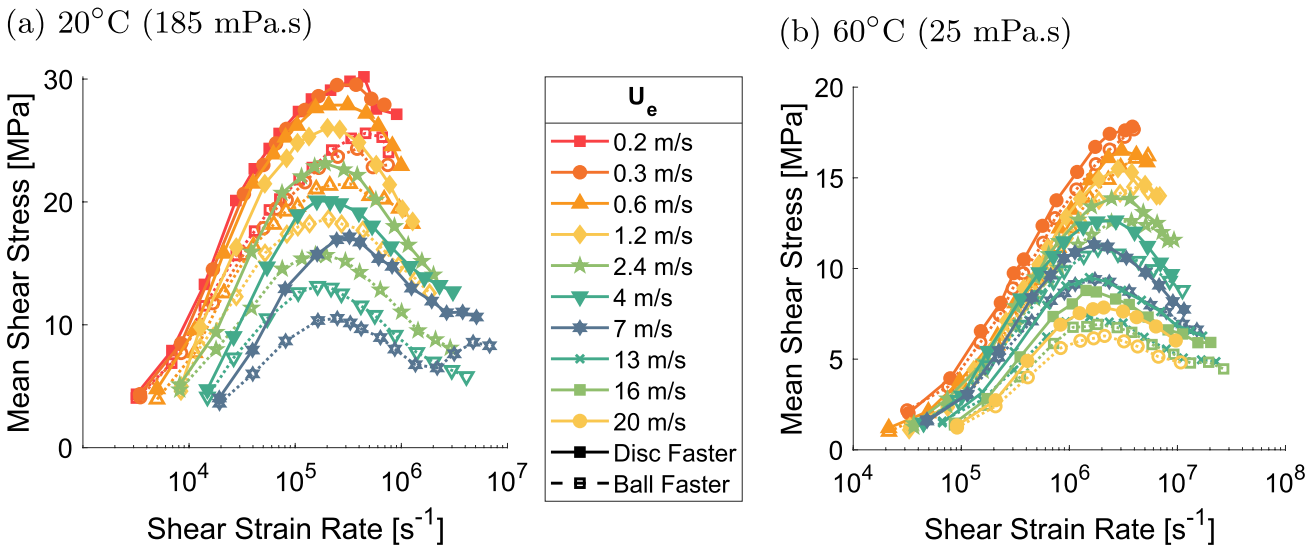


Fig. 17 Mean shear stress $\bar{\tau}$ vs shear strain rate $\dot{\gamma}$ for higher-viscosity Mineral Oil at (**a**) 20°C and (**b**) 60°C, steel ball on glass disc at 50 N load for selected speeds, showing the effect of viscosity on shear stress under forward and reverse sliding

3.6 Shear Stress Response to Viscosity and Fluid Composition

Increasing the bulk fluid temperature, and hence reducing viscosity, has the effect of increasing shear strain rate due to the reduced film thickness, while also lowering friction in-contact, so reducing shear stress. The lower shear stress delays the onset of shear-thinning to higher strain rates. Mean shear stress vs strain rate is shown for three temperatures in Fig. 16, for two fluids. For the PAO, the forward and reverse sliding cases correspond very closely, whereas for the Group I oil they differ significantly across the whole speed range at low temperature, due to the traction coefficient difference shown in Fig. 14 for this fluid.

Figure 17 examines the mean shear stress vs shear strain for a higher-viscosity heavy mineral oil, for two temperatures. The shear stress in forward sliding is again higher than in the reverse direction and this discrepancy widens as entrainment speed increases. Note that the sequence of measurements was such that each slide-roll ratio was completed before moving on to the next, and that all slide-roll ratios were measured for a particular speed in order of increasing

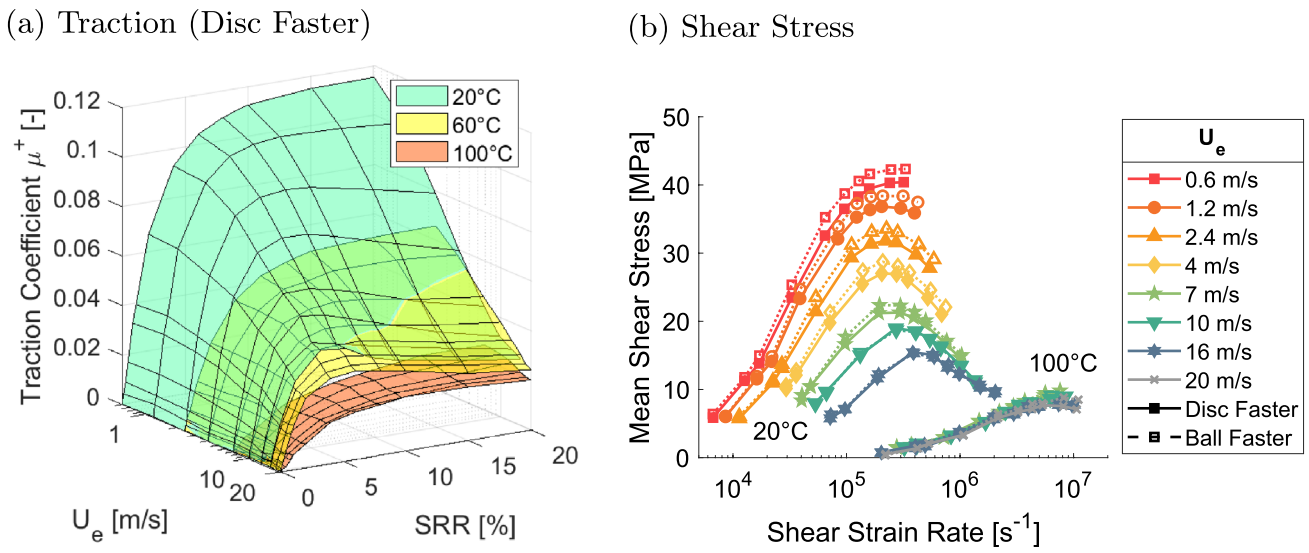


Fig. 18 Traction vs U_e and SRR (**a**) and mean shear stress $\bar{\tau}$ vs shear strain rate $\dot{\gamma}$ (**b**) of the traction fluid Santotrac 50 for SRR≤20%, steel-on-glass

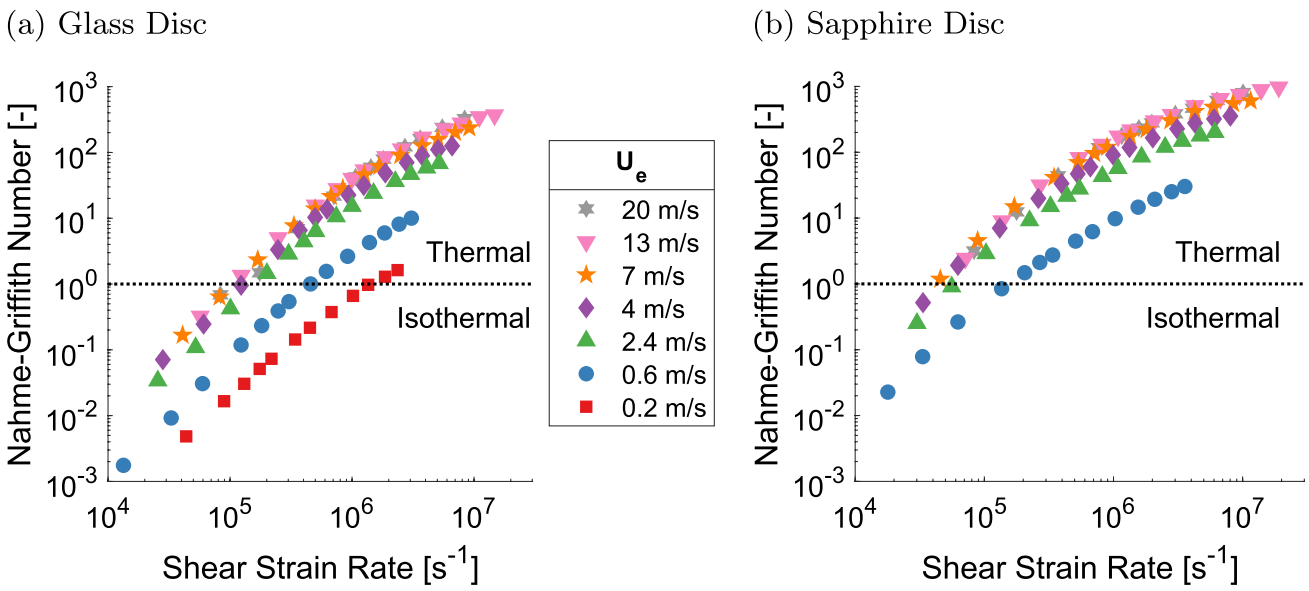


Fig. 19 Nahme-Griffith number Na vs shear strain rate for the data from Fig. 13

SRR, before moving on to the next entrainment speed. This means that the forward and reverse traction measurements (to give $\bar{\tau}$) for each SRR (hence for each $\dot{\gamma}$) were taken just seconds apart. The thermal inertia of the oil sump and steel casing are such that single-degree bulk temperature changes take minutes to come into effect, so the thermal contribution to the difference between forward and reverse traction seen here is certainly confined to contact length-scales (µm) and time-scales (µs).

Traction measurements and calculated mean shear stresses for the traction fluid Santotrac 50 are shown in Fig. 18. The rheology of this fluid differs significantly from the others studied here in that the fluid exhibits a far stronger pressure-viscosity response, and this leads to higher film thickness and to very high traction coefficients, which rise sharply in a Newtonian fashion with sliding speed and then (at low entrainment speeds) remain approximately constant, exhibiting a limiting shear stress [30]. For these high traction coefficients, sliding speeds were limited by the torque capacity of the ball drive motor, and so only slide-roll ratios below 20% were measured for this fluid.

4 Discussion

As entrainment speed increases, it is seen that:

- Film thickness falls below the isothermal prediction of the form $h_c \propto U_e^{0.68}$. At lower viscosities, the effect is postponed to higher speeds.
- Film thickness and traction both depend increasingly on sliding direction. In a steel-on-sapphire contact, this dependence is stronger than in a steel-on-glass contact at the same load.
- Traction is increased in the Newtonian regime (at very low SRRs), and reduced elsewhere. The extent of this change strongly depends on viscosity—for viscosities around 4 cSt, traction almost does not depend on speed in the range 4–20 m/s.
- The 'plateau', shear-thinning, and Newtonian regimes are eventually absorbed by the thermoviscous regime, in which case traction is globally reduced, becoming a monotonically increasing function of sliding speed.

A prevailing question is, what is role of inlet heating in modifying traction and film thickness? Both inlet shear heating, and heating of the lubricant in the inlet by the solids must be considered (at high shear rates we may safely neglect the contribution of compression heating [31, 32]). Classical flash temperature analysis has followed Jaeger [33], who assumed the contact is bounded by two semi-infinite bodies whose inlet temperatures match the nominal bulk fluid temperature. At high speeds in a ball-on-disc tribometer with significant heat dissipation from the contact however, the surface temperatures at the inlet may become considerably higher than the bulk fluid temperature. The thermal analysis presented in Appendix B concludes that the contact track is unable to reject heat to the rest of the ball fast enough for the surface temperature to have relaxed to the bulk temperature each time it re-enters the contact. The ball surface temperature will therefore rapidly rise during the test until a steady-state is reached, a circumstance which was observed during the tests by significant bulk fluid temperature rise in the vicinity of the ball at high speeds. Active cooling of the oil sump was employed to counteract this. It is worthy of note that high-speed EHD contacts in gears and bearings also recirculate, and the design of these machine elements will determine at what speed the thermal response of the solids becomes significant.

The Nahme-Griffith number Na describes the ratio of temperature rise caused by shearing to temperature rise required for significant ($\mathcal{O}(1)$) viscosity increase

$$\mathrm{Na} = \beta \frac{\tau \dot{\gamma} h_c^2}{\kappa_{\mathrm{oil}}} \tag{15}$$

where β is the temperature coefficient of viscosity taken here (at atmospheric pressure) as

$$\beta = -\frac{1}{\eta}\frac{\partial \eta}{\partial T} = \frac{B}{\left(T - T_0\right)^2} \tag{16}$$

when Na > 1, the thermal viscosity reduction may be considered to make a significant change to contact traction. Na is plotted in Fig. 19 for the results from Fig. 13, showing that for steel-on-glass, at the lowest speeds there is a clear isothermal region up to shear rates $\sim 10^6$, whereas for steel-on-sapphire, in almost all cases the fluid viscosity is strongly influenced by temperature change in contact (the Nahme-Griffith number does not, of course, account for the effect of inlet shear heating or solid recirculation). The results for steel-on-glass case at least, with a wide isothermal region, show that the Eyring response is not just a thermal artefact. Fluid viscosity and entrainment speed therefore also fundamentally influence the contact temperature rise in this set-up, as the ball and disc surface convective heat transfer coefficients outside the contact strongly depend on viscosity and speed (particularly as the flow transitions from laminar to turbulent). It should also be noted that the value of fluid thermal conductivity $\kappa_{\mathrm{oil}} = 0.15$ W/mK used in the calculation of Na, and of L_T in the Gupta correction, was an approximation which did not account for the variation in κ_{oil} with temperature, fluid type, and most significantly, pressure [34]. The true value is not expected however to deviate from 0.15 W/mK by a factor of more than 2 for the steel-on-glass contact, and this does not significantly influence the conclusions regarding the Gupta correction and the Nahme-Griffith number made here.

The traction measurements clearly display the four distinct regimes detailed in the numerical study of Habchi, Bair and Vergne [35], namely linear, shear-thinning, plateau and thermoviscous. A key qualitative difference between their results and the experimental data obtained here however is the change in concavity of the traction curves in the thermoviscous region (see Fig. 9), indicating a second plateau at very high sliding speed. This difference is corroborated by the experimental results from Wedeven's WAM tribometer at lower speeds presented by those same authors in Björling et al. [19], which display the same change in concavity as the results presented here. The discrepancy is concluded by Björling to be attributable to the numerical treatment of fluid rheology. The higher-speed measurements here, combined with simultaneous film thickness measurement, enable the effect to be examined with respect to mean shear stress and shear strain rate.

Firstly, the thermal reduction in shear stress appears to act in all cases before a limiting shear stress is reached—the shear stress curves have quite sharp peaks even at low speeds in Fig. 17, and the deviation from the Eyring line in Fig. 13

coincides very closely with the point at which the Nahme-Griffith number rises above unity in Fig. 19.

Secondly, it appears that in the thermoviscous region, thermal recirculation by the specimens (even, in Fig. 17a, at quite low speeds) has a highly significant effect on traction, leading to vastly different traction coefficients and shear stresses for equivalent shear strain in forward and reverse sliding for some fluids. Regrettably, it is rarely made clear in the literature whether measurements of forward, reverse, or an average traction value are being quoted—these three metrics may produce very different values. In some cases, choosing the average traction would widen the shear stress plateau, as the thermal reduction causes a local maximum at different shear rates for the two sliding directions, giving the illusion of limiting shear stress behaviour. In addition, the confounding effect of macroscopic viscous drag on the traction measurement increases at high speeds under high-sliding conditions in both the EHD-HS and WAM tribometers. The result may therefore be an artefact of the ball-on-disc experimental set-up rather than the fluid rheology.

Thirdly, it appears, although the relevant shear rates were not reached in this study, that for very high shear rate ($\sim 10^8$ s^{-1}) there is some thermoviscous limit to which the mean shear stress converges at all speeds. For the fluids studied, regardless of viscosity, this appears to lie somewhere between 5 and 10 MPa. In this limit, it is tentatively proposed that the viscosity in-contact would become highly non-uniform in the entrainment direction and the central plateau would shrink. Toward the thermoviscous limit, the exponential decrease in viscosity with temperature would outstrip the lower-order dependence of temperature on shear strain rate, yielding approximately constant traction at very high-sliding as shear-heating competes with shear thinning. This is however only conjecture—the fluid rheological response under these extreme conditions is a subject of considerable debate, and experiments which could cool the fluid fast enough to obtain stable steady-state conditions and take relevant temperature measurements would be challenging. Only experimental work under EHD-representative pressures and shear stresses, for example in actual EHD contacts, is currently capable of definitively resolving this question—the use of the infrared mapping technique [36, 37] with the new EHD-HS for example, would go some way to addressing this.

4.1 Difference in Traction with Sliding Direction

It can be seen from Fig. 13 that at high viscosities, even at modest sliding speeds within the Newtonian regime, shear stress is lower at high entrainment speeds, highlighting the thermal coupling between inlet shear and shear in-contact. (At low viscosities by contrast, the Newtonian regime proliferates to much higher strain rates ($\sim 10^7$ s^{-1}) on account of the shear stress remaining well below τ_e, which here is around 4.0 MPa, and the effect of entrainment speed is greatly reduced.)

The consistent discrepancy between film thickness in the positive and negative sliding cases is also relevant. By their nature, the specimens in the EHD-HS see the contact repeatedly pass over any given point on the track, and the pass frequency increases with speed. A speed must exist where the specimen surface does not have time to cool to (nearly) the far-field temperature before it is recirculated into the contact, and in this case the temperature profile of the contact

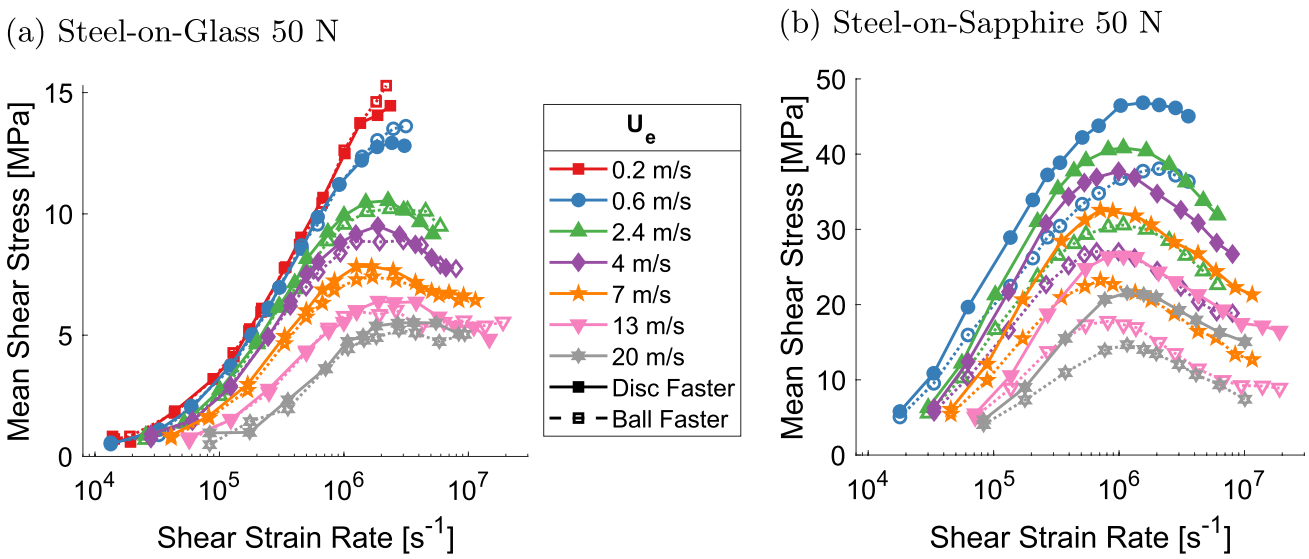


Fig. 20 Mean shear stress $\bar{\tau}$ vs shear strain $\dot{\gamma}$ for PAO5 (Group IV) with a steel ball on glass disc (**a**) and sapphire disc (**b**) at 20°C and 50 N load for selected speeds showing both forward and reverse sliding directions

must change by comparison to the hypothetical case where the material ahead of the contact is always at the far-field temperature. This is different for each surface, and depends on the recirculation time, which is a function of the both the geometry and the speeds—here the disc track is between 3.6 and 4.6 times longer (depending on chosen disc track radius) than the ball track, and although the thermal bulk of the glass is larger in total, it has a much lower thermal conductivity than steel [38]. All of these conditions imply the ball would take on heat more rapidly (owing to its higher thermal diffusivity), and would lose it by convection less rapidly elsewhere (owing to its smaller surface area per unit volume) than the glass disc, if all else were equal.

Under sliding conditions however, a longer portion of the track on the faster surface is in contact per unit time than on the slower surface, affording the faster surface greater opportunity to take on heat. Consequently, if this surface becomes considerably hotter than the far-field temperature, there is less opportunity for the contact to cool via this surface, and near to the inlet, the entrained fluid may be heated. The ball, with its shorter recirculation time and higher diffusivity, is therefore likely to assume a higher upstream temperature, and therefore to give a higher temperature rise in-contact when it is the faster surface. The test constantly oscillates between forward and reverse sliding conditions, spending only a few seconds in each, too short a time for the bulk fluid temperature to change significantly, so this effect is certainly contact-local. The film thickness is lower in reverse sliding by up to 25% in some cases, the magnitude of the difference increasing with speed (shorter recirculation time) and SRR (higher heat flux).

It is therefore unsurprising that the effect of reversing sliding direction on traction and mean shear stress is considerable in cases of high shear stress, and in cases where a significant heat flux is likely to be very unequally partitioned between bodies. For all fluids except Santotrac 50, when the ball is faster, lower or equal traction is measured compared to the disc-faster case. Figure 20 shows the disc-faster shear stresses from Fig. 13 overlaid with the ball-faster case. For steel-on-sapphire with PAO5 at 20°C, the traction difference is quite substantial. Figure 17 shows the same is true of the high-viscosity mineral oil. The ball-faster case also produces lower film thickness, which implies higher inlet temperature, and hence lower viscosity in-contact, leading to lower traction. Both traction and film thickness differences are greater at higher entrainment speeds.

A notable exception is the traction fluid, for which the ball-faster case imparts slightly higher traction, and the effect is instead strongest at low speeds, although the film thickness trend remains the same as for the other fluids: ball-faster incurs (very slightly) lower film thickness. This suggests that in the case of the very high traction coefficients and therefore heat fluxes for Santotrac 50 at low speeds, the recirculated heat is small compared to the flash heating, and so the ball-faster condition enables the contact to run cooler on account of the greater thermal conductivity of steel. The thermal conductivity of Santotrac 50 was measured by Larsson [34] to be about half of that for other common lubricating base oils, and this effect proliferates at high pressures, which could further increase the influence of heat storage within the film, and diminish the effect of surface heat recirculation.

At high speeds, increasing the SRR (which strongly increases flash temperature) has a significant impact on film thickness, and this effect is stronger in reverse sliding, suggesting that the recirculation of shear heat from the contact into the inlet is responsible for this. It should be noted however that SRRs in the range between 60 and 200% are unusual in machine elements, so the influence of high-sliding conditions on EHL film thickness is not commonly seen in real applications. This effect is generally less significant than the influence of entrainment speed on film thickness, compared to the isothermal case.

4.2 Viscoelasticity

The Johnson and Tevaarwerk model [39] expresses shear strain rate $\dot{\gamma}$ according to Eq. 17, as the sum of the viscous (sinh term) and elastic ($\frac{\mathrm{d}\tau}{\mathrm{d}t}$ term) response.

$$\dot{\gamma} = \frac{\tau_e}{\eta_p} \sinh\left(\frac{\tau}{\tau_e}\right) + \frac{1}{G_e}\frac{\mathrm{d}\tau}{\mathrm{d}t} \tag{17}$$

The relative strength of the elastic response is indicated by the Deborah number D (the ratio of fluid relaxation time to transit time), with elastic shear significantly lowering mean shear stress where $D > 1$. A procedure for evaluating the Deborah number for the tests on PAO5 in this study is presented in Appendix C, which shows that the assumptions made are likely to significantly overestimate D. Despite this, D is found to be less than unity in all cases except for the lowest temperature with the sapphire disc, where the value remains below 4. Considering the inevitable underestimation of the shear modulus by fitting to traction measurements, it is likely that $D < 1$ holds for PAO5 at both contact pressures tested. Viscoelasticity is therefore considered to remain insignificant in this study for the results with PAO. The effect of viscoelasticity on EHL traction is not generally negligible however. Viscoelastic effects may become more significant at high entrainment speeds when transit times are short, and at high shear stresses, particularly for higher-viscosity, more strongly piezoviscous lubricants at high contact pressures. Definitive evaluation of these effects relies on a reliable estimate of η_p and G_p which was not available for the mineral oils tested.

4.3 Measurement Limitations

The assumption that, in the F_0^+ and analogous F_0^- cases, the zero-sliding traction force from the contact is negligible, may break down at high entrainment speed, where there is clearly a viscous (inlet shear) contribution to traction. The Poisseuille contribution (proportional to the streamwise pressure gradient) is also expected to change as the film thickness and pressure profiles change shape with speed. This may account for some of the reduction in traction at low-sliding but high-entrainment speed conditions. In addition, the spin in the contact, resulting from perpendicular axes of rotation of the ball and disc, may influence the traction behaviour, although the difference in entrainment speed from one side of the contact to the other is very slight, estimable by the ratio of the contact width to the disc track radius, which is less than 1%. The small contribution of both of these effects to traction force is not expected to significantly influence the trends presented except at very small slide-roll ratios of less than 2% in magnitude, and no attempt is made here to quantify or compensate for these. The values for traction coefficient presented herein should therefore be considered in deference to these assumptions.

5 Conclusions

A high-speed optical tribometer has been employed to simultaneously measure film thickness and traction in an elastohydrodynamic contact up to 20 m/s for the first time. Film thicknesses were measured using ultra-thin-film interferometry, and traction was measured using a novel traction measurement procedure developed in this study. The technique has been used to map traction and film thickness for entrainment speeds between 0.2 and 20 m/s, and SRRs between 0 and 100%, for base fluids representing those in common use in transmissions, spanning API Groups I–IV and including a traction fluid. The main findings are:

- The results at low speeds show good agreement with existing traction and film thickness measurements for these fluids.
- The simultaneous measurement of film thickness and traction has enabled mean shear stress and mean shear strain rate to be calculated from measurements, enabling the thermal dependence of the mean shear stress in the plateau and thermoviscous traction regimes to be examined.
- At entrainment speeds above a certain threshold (the exact value of which depends on the fluid type and viscosity) the measured film thickness is lower than that predicted using classical isothermal EHL regression equations. A difference of up to 100% of the measurement was found at the highest speeds.
- The deviation from the isothermal film thickness prediction is found for all fluids to match the prediction of Gupta quite well in pure rolling, but for rolling-sliding contacts Gupta predicts considerably lower film thicknesses than those measured.
- The reduction in film thickness was observed under fully-flooded conditions, so was not caused by starvation in any of the tests here.
- The shear rate at which mean shear stress deviates from the Johnson and Tevaarwerk model is that at which the Nahme-Griffith number exceeds unity, up to a shear stress of 35 MPa in a steel-on-sapphire contact with PAO5. Consequently no isothermal behaviour attributable to a limiting shear stress is seen under these conditions.
- Both traction and film thickness depend on sliding direction in a high-speed ball-on-disc set-up where the bounding surfaces are made of dissimilar materials and the specimens rotate at different angular frequencies. The

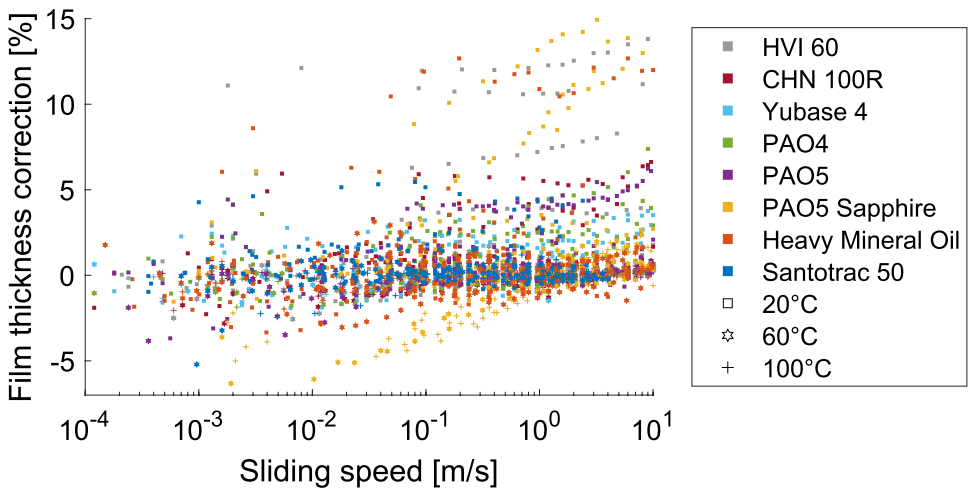


Fig. 21 Film thickness correction $\left[\eta(T_{\text{nom.}})/\eta(T_{\text{meas.}})\right]^{0.68}$ vs sliding speed for all fluids tested showing only a small minority of measurements incur a substantial correction due to excursions in temperature at high sliding speeds

effects of sliding direction were found to increase with sliding speed, Hertz pressure, and fluid viscosity. The film thickness difference is significant in this study above 20% SRR. The traction difference is significant in cases where the mean shear stress exceeds 4.0 MPa. The magnitude of the difference is likely to depend on the relative thermal resistances of the two contacting bodies (which varies significantly among tribometers), and their relative recirculation rates, which varies with specimen geometry, entrainment and sliding speeds.

- The results show that at speeds which are commonly encountered in electric vehicle transmissions, aerospace, and other high-speed applications, the oil film thickness and traction behaviour differs significantly from the conventional theory derived from isothermal observations at low and moderate speeds. These results can therefore help to inform better design of such high-speed systems, not least in optimising lubricant selection.

Appendix A

Correction to Measured Film Thickness for Bulk Temperature Variation

Temperature control of the oil reservoir to within ±1°C is achieved below 10 m/s, and globally within ±5°C of the nominal temperature. The expected film thickness error incurred by the measured bulk fluid temperature deviation, assuming $h_c \propto \eta^{0.68}$, is up to 2.5% at 100°C, and up to 12% at 20°C for the steel-on-glass tests. The film thickness measurements have therefore been corrected using Eq. 18, which accounts for the viscosity change as a result of the measured deviation from the nominal value, where $\eta(T)$ is the dynamic viscosity predicted by the VFT relationship at temperature T (Eq. 6), $T_{\text{meas.}}$ is the fluid temperature measured by the temperature probe close to the ball, and $T_{\text{nom.}}$ is the nominal fluid temperature, i.e. 20°C, 60°C or 100°C.

$$h_c = h_{c_{\text{meas.}}} \left(\frac{\eta(T_{\text{nom.}})}{\eta(T_{\text{meas.}})} \right)^{0.68} \tag{18}$$

For the majority of measurements presented, this correction changes the film thickness by less than 0.5%. The magnitude of the correction exceeds 5% for only 4% of the measurements (see Fig. 21), principally those at the highest sliding speeds with the higher-traction mineral oils. The correction is applied to improve the quality of the comparisons made between tests on different fluids, but even without this correction, the conclusions regarding the considerably greater discrepancy between these measurements and the predictions of Chittenden and Gupta remain unchanged.

Appendix B

Surface Temperature Rise

Consider the Biot number Bi (Eq. 19), which examines the relative strength of convective and conductive modes at the ball surface, where κ is the thermal conductivity of steel.

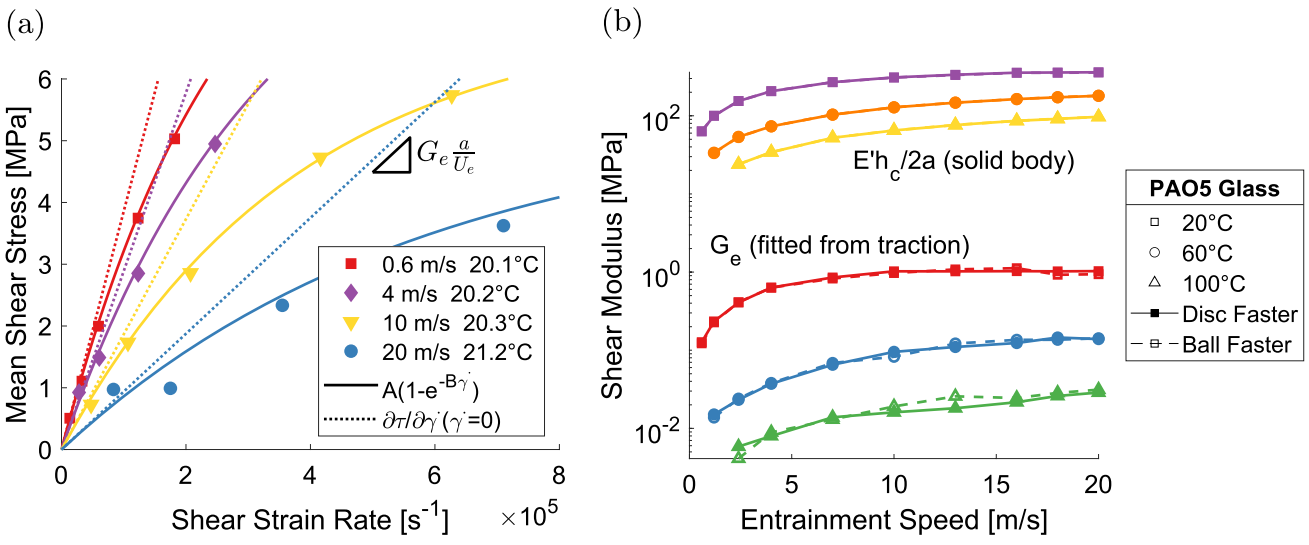


Fig. 22 **a** Eq. 23 fitted to $\bar{\tau}$ vs $\dot{\gamma}$ for SRR < 5% at four entrainment speeds, for PAO5 with glass disc, showing tangent to curve at $\dot{\gamma} = 0$ and gradient used to find shear modulus G_e. **b** shows the values of G_e calculated and compares them to the reciprocal of the solid elastic compliance term $E'h_c/2a$

$$\mathrm{Bi} = \frac{h}{\kappa} L_c \tag{19}$$

We shall assume a convective heat transfer coefficient $h \sim 500\ \mathrm{W/m^2K}$ outside the contact, and conservatively take the characteristic length L_c as the ball radius (in reality the predominant thermal gradients are seen across much shorter length-scales). This produces $\mathrm{Bi} \sim 0.2$, and so convection is slower than conduction, which means that heat diffusion within the ball is the predominant path for heat energy from the contact track, before eventually being rejected elsewhere on the ball surface by convection. Conduction via the quill shaft which drives the ball can safely be neglected on account of its geometry.

Following Archard [40], we next consider a characteristic timescale for heat diffusion from the contact into the ball specimen t_d (Eq. 20), where a is the contact half-width, and χ is the thermal diffusivity of steel. Consider also the time taken for the contact to traverse the circumference of the ball once, the recirculation time t_r.

$$t_d = \frac{a^2}{2\chi} \qquad t_r = \frac{2\pi R}{U_1} \qquad \frac{t_r}{t_d} = \frac{4\pi\chi R}{a^2 U_1} \tag{20}$$

We find that, for $U_{\mathrm{ball}} \sim 20$ m/s, $t_r/t_d \sim 1$, and so for the EHD-HS which uses a 3/4" ball, and ignoring convection on account of the low Biot number, we conclude that the contact track is unable to reject heat to the rest of the ball fast enough for the surface temperature to have relaxed to the bulk temperature each time it re-enters the contact.

Appendix C

Deborah Number

The Deborah number D is given by

$$D = \frac{\eta_p U_e}{2aG_e} \tag{21}$$

The equivalent shear modulus G_e, accounting approximately for the additional effect of elastic deformation in the solids, is found from the parallel combination of the fluid shear modulus G_p, and the reduced contact modulus multiplied by the aspect ratio of the contact [41].

$$\frac{1}{G_e} = \frac{1}{G_p} + \frac{2a}{E'h_c} \tag{22}$$

The conclusions drawn about the significance of viscoelasticity based on the value of D strongly depend on the assumptions made in evaluating G_p and η_p, both of which are strong functions of temperature, pressure, and molecular structure. In lieu of a model for G_p, the exponential in Eq. 23 is fitted to the values of $\bar{\tau}$ and $\dot{\gamma}$ calculated from the reported traction measurements where SRR < 5% (Fig. 22a), and A and B are positive fitting coefficients. G_e is then obtained from Eq. 24, according to the method used by Loewenthal and Rohn [42].

$$\bar{\tau} \approx A\left(1 - e^{-B\dot{\gamma}}\right) \tag{23}$$

$$G_e \approx \frac{U_e}{a} \left.\frac{\partial \bar{\tau}}{\partial \dot{\gamma}}\right|_{\dot{\gamma}=0} \approx AB\frac{U_e}{a} \tag{24}$$

This method has the disadvantage that it requires the Deborah number to be high (Johnson and Tevaarwerk [39] suggest $D > 100$), which for most fluids requires pressures not achieved in this study. However, if it is the case that D is low, then viscous shear superposes with elastic shear and the film appears more compliant, reducing G_e and increasing D. This means the values of D calculated here are in their upper limit.

It can be seen in Fig. 22b that the reciprocal elastic compliance $E'h_c/2a$ is over 2 orders of magnitude higher than the value of G_e calculated from the fits to traction measurements, whereas we might expect them to be of comparable order, especially given the relatively low E' of the steel-glass contact. This supports the hypothesis that if D is low, and viscous shear predominates, the 'shear modulus' is underestimated. G_p is expected to increase approximately linearly with pressure (and the gradient is reduced by increasing temperature), so higher temperatures produce lower shear moduli. The fact that the 'shear modulus' appears to increase with speed here (instead of remaining constant, as would be expected isothermally, or decreasing due to inlet shear heating at high speeds) also supports this hypothesis.

The mean piezoviscous viscosity in the contact η_p is calculated using the improved Yasutomi correlation fitted to viscosity measurements of PAO4 at high pressure by Bair [43]. Firstly it is assumed that the PAO5 used in this study bears sufficient rheological similarity to PAO4 that its viscosity can be estimated from fits for PAO4 by adjusting the temperature given to the Yasutomi correlation (downwards) to that at which PAO4 has the same atmospheric-pressure viscosity as PAO5 at the nominal temperature. Secondly, the pressure assumed is the mean Hertz pressure. These two approximations allow η_p to be estimated to within an order of magnitude.

Supplementary Information The online version contains supplementary material available at https://doi.org/10.1007/s11249-024-01894-w.

Acknowledgements Alexander MacLaren wishes to thank Roland Jones and Eliane Gendreau for their technical and moral support with this work. The authors would like to thank Tom Welham, Clive Hamer

and John Hutchinson of PCS Instruments who were responsible for the development of the EHD-HS.

Author Contributions AM and AK were both responsible for the conceptualisation of the study. AM was reponsible for the development of the method, the execution of the tests, the preparation of figures and the writing of the manuscript. All authors reviewed the manuscript.

Funding The authors gratefully acknowledge financial support from UKRI EPSRC via a CASE award (Award Number EP/T51780X/1), and additional funding from Valvoline Inc.

Data Availability Supplementary Data are available online, and will be made available in raw form on reasonable request to the corresponding author or to tribology@imperial.ac.uk.

Declarations

Conflict of interest The authors have no relevant financial or non-financial interests to declare.

Open Access This article is licensed under a Creative Commons Attribution 4.0 International License, which permits use, sharing, adaptation, distribution and reproduction in any medium or format, as long as you give appropriate credit to the original author(s) and the source, provide a link to the Creative Commons licence, and indicate if changes were made. The images or other third party material in this article are included in the article's Creative Commons licence, unless indicated otherwise in a credit line to the material. If material is not included in the article's Creative Commons licence and your intended use is not permitted by statutory regulation or exceeds the permitted use, you will need to obtain permission directly from the copyright holder. To view a copy of this licence, visit http://creativecommons.org/licenses/by/4.0/.

References

1. Spikes, H.A.: Sixty years of EHL. Lubr. Sci. **18**(4), 265–291 (2006). https://doi.org/10.1002/LS.23
2. Lugt, P.M., Morales-Espejel, G.E.: A review of Elasto-hydrodynamic lubrication theory. Tribol. Trans. **54**(3), 470–496 (2011). https://doi.org/10.1080/10402004.2010.551804
3. Gohar, R.: Elastohydrodynamics, 2nd edn. Imperial College Press, London (2001)
4. Lubrecht, A.A., Venner, C.H., Colin, F.: Film thickness calculation in Elasto-hydrodynamic lubricated line and elliptical contacts: the Dowson, Higginson, Hamrock contribution. Proc. Inst. Mech. Eng., Part J: J. Eng. Tribol. **223**, 511–515 (2009). https://doi.org/10.1243/13506501JET508
5. Foord, C.A., Hammann, W.C., Cameron, A.: Evaluation of lubricants using optical elastohydrodynamics. ASLE Trans. **11**(1), 31–43 (1968). https://doi.org/10.1080/05698196808972206
6. Gupta, P.K., Cheng, H.S., Zhu, D., Forster, N.H., Schrand, J.B.: Viscoelastic effects in MIL-L-7808-type lubricant, part I: analytical formulation. Tribol. Trans. **35**(2), 269–274 (1992). https://doi.org/10.1080/10402009208982117
7. Shore, J.F., Christodoulias, A.I., Kolekar, A.S., Lockwood, F.E., Kadiric, A.: Prediction of Electric Vehicle Transmission Efficiency Using a New Thermally Coupled Lubrication Model. SAE Technical Papers (2022). https://doi.org/10.4271/2022-01-5026
8. Shore, J.F., Kolekar, A.S., Ren, N., Kadiric, A.: An investigation into the influence of viscosity on gear churning losses by considering the effective immersion depth. Tribol. Trans. (2023). https://doi.org/10.1080/10402004.2023.2247041
9. Takabi, J., Khonsari, M.M.: On the thermally-induced failure of rolling element bearings. Tribol. Int. **94**, 661–674 (2016). https://doi.org/10.1016/J.TRIBOINT.2015.10.004
10. Jafari, S., Nikolaidis, T., Heerden, A.S.J., Lawson, C.P., Bosak, D.: Physics-based thermal model for power gearboxes in geared turbofan engines. Proc. ASME Turbo Expo **1**, 1–7 (2020). https://doi.org/10.1115/GT2020-14637
11. Greenwood, J.A.: An extension of the Grubin theory of elasto-hydrodynamic lubrication. J. Phys. D Appl. Phys. **5**(12), 2195–2211 (1972). https://doi.org/10.1088/0022-3727/5/12/309
12. Cameron, A.: Righting a 40-year-old wrong. Tribol. Int. **18**(2), 92 (1985). https://doi.org/10.1016/0301-679x(85)90038-6
13. Wheeler, J.-D., Vergne, P., Fillot, N., Philippon, D.: On the relevance of analytical film thickness EHD equations for isothermal point contacts: qualitative or quantitative predictions? Friction **4**(4), 369–379 (2016). https://doi.org/10.1007/s40544-016-0133-7
14. Spikes, H., Jie, Z.: History, origins and prediction of Elastohydrodynamic friction. Tribol. Lett. **56**(1), 1–25 (2014). https://doi.org/10.1007/S11249-014-0396-Y
15. Bair, S., Vergne, P., Kumar, P., Poll, G., Krupka, I., Hartl, M., Habchi, W., Larsson, R.: Comment on history, origins and prediction of Elastohydrodynamic friction by Spikes and Jie. Tribol. Lett. **58**(1), 1–8 (2015). https://doi.org/10.1007/S11249-015-0481-X
16. Bair, S.: Is it possible to extract the pressure dependence of low-shear viscosity from EHL friction? Tribol. Int. **151**(April), 106454 (2020). https://doi.org/10.1016/j.triboint.2020.106454
17. Bair, S.: A traction (friction) curve is not a flow curve. Lubricants **10**(9), 221 (2022). https://doi.org/10.3390/LUBRICANTS10090221
18. Spikes, H., Zhang, J.: Reply to the Comment by Scott Bair, Philippe Vergne, Punit Kumar, Gerhard Poll, Ivan Krupka, Martin Hartl, Wassim Habchi, Roland Larson on History, Origins and prediction of Elastohydrodynamic friction by Spikes and Jie in tribology letters. Tribol. Lett. **58**(1), 1–6 (2015). https://doi.org/10.1007/S11249-015-0483-8
19. Björling, M., Habchi, W., Bair, S., Larsson, R., Marklund, P.: Towards the true prediction of EHL friction. Tribol. Int. **66**, 19–26 (2013). https://doi.org/10.1016/j.triboint.2013.04.008
20. Ardah, S., Profito, F.J., Reddyhoff, T., Dini, D.: Advanced modelling of lubricated interfaces in general curvilinear grids. Tribol. Int. **188**, 108727 (2023). https://doi.org/10.1016/J.TRIBOINT.2023.108727
21. Cheng, H.S.: A refined solution to the thermal-Elastohydrodynamic lubrication of rolling and sliding cylinders. ASLE Trans. **8**(4), 397–410 (1965). https://doi.org/10.1080/05698196508972110
22. Cheng, H.S., Sternlicht, B.: A numerical solution for the pressure, temperature, and film thickness between two infinitely long, lubricated rolling and sliding cylinders, under heavy loads. J. Basic Eng. **87**(3), 695–704 (1965). https://doi.org/10.1115/1.3650647
23. Wilson, W.R.D., Sheu, S.: Effect of inlet shear heating due to sliding on Elastohydrodynamic film thickness. J. Lubr. Technol. **105**(2), 187–188 (1983). https://doi.org/10.1115/1.3254563
24. Pandey, R.K., Ghosh, M.K.: Thermal effects on film thickness and traction in rolling/sliding EHL line contacts—an accurate inlet zone analysis. Wear **192**(1–2), 118–127 (1996). https://doi.org/10.1016/0043-1648(95)06778-7
25. Hili, J., Olver, A.V., Edwards, S., Jacobs, L.: Experimental investigation of Elastohydrodynamic (EHD) film thickness behavior at high speeds. Tribol. Trans. **53**(5), 658–666 (2010). https://doi.org/10.1080/10402001003658326
26. Johnston, G.J., Wayte, R., Spikes, H.A.: The measurement and study of very thin lubricant films in concentrated contacts. Tribol.

Trans. **34**(2), 187–194 (1991). https://doi.org/10.1080/10402009108982026
27. Liang, H., Guo, D., Reddyhoff, T., Spikes, H., Luo, J.B.: Influence of thermal effects on Elastohydrodynamic (EHD) lubrication behavior at high speeds. Sci. China Technol. Sci. **58**(3), 551–558 (2015). https://doi.org/10.1007/s11431-014-5564-7
28. Chittenden, R.J., Dowson, D., Dunn, J.F., Taylor, C.M.: A theoretical analysis of the isothermal elastohydrodynamic lubrication of concentrated contacts. I. Direction of lubricant entrainment coincident with the major axis of the Hertzian contact ellipse. Proc. R. Soc. London A Math. Phys. Sci. **397**(1813), 245–269 (1985). https://doi.org/10.1098/RSPA.1985.0014
29. Vogel, H.: The law of the relation between the viscosity of liquids and the temperature. Phys. Z. **22**(1), 645–646 (1921)
30. Fang, N., Chang, L., Webster, M.N., Jackson, A.: A non-averaging method of determining the rheological properties of traction fluids. Tribol. Int. **33**(11), 751–760 (2000). https://doi.org/10.1016/S0301-679X(00)00116-X
31. Reddyhoff, T., Spikes, H.A., Olver, A.V.: Compression heating and cooling in Elastohydrodynamic contacts. Tribol. Lett. **36**(1), 69–80 (2009). https://doi.org/10.1007/S11249-009-9461-3
32. Habchi, W., Vergne, P.: On the compressive heating/cooling mechanism in thermal Elastohydrodynamic lubricated contacts. Tribol. Int. **88**, 143–152 (2015). https://doi.org/10.1016/J.TRIBOINT.2015.03.025
33. Jaeger, J.C.: Moving sources of heat and the temperature at sliding contacts. J. Proc. R. Soc. N. S. W. **76**(3), 203–224 (1942). https://doi.org/10.5962/p.360338
34. Larsson, R., Andersson, O.: Lubricant thermal conductivity and heat capacity under high pressure. Proc. Inst. Mech. Eng., Part J: J. Eng. Tribol. **214**(4), 337–342 (2000). https://doi.org/10.1243/1350650001543223
35. Habchi, W., Bair, S., Vergne, P.: On friction regimes in quantitative elastohydrodynamics. Tribol. Int. **58**, 107–117 (2013). https://doi.org/10.1016/J.TRIBOINT.2012.10.005
36. Spikes, H.A., Anghel, V., Glovnea, R.: Measurement of the rheology of lubricant films within elastohydrodynamic contacts. Tribol. Lett. **17**(3), 593–605 (2004). https://doi.org/10.1023/B:TRIL.0000044509.82345.16/METRICS
37. Lu, J.: Experimental and Numerical Analysis of Thermal Elastohydrodynamic Contacts. PhD thesis, Imperial College London (2019)
38. Reddyhoff, T., Schmidt, A., Spikes, H.: Thermal conductivity and flash temperature. Tribol. Lett. **67**(1), 1–9 (2019). https://doi.org/10.1007/s11249-018-1133-8
39. Johnson, K.L., Tevaarwerk, J.L.: Shear behaviour of elastohydrodynamic oil films. Proc. R. Soc. London Ser. A **356**(1685), 215–236 (1977). https://doi.org/10.1098/rspa.1977.0129
40. Archard, J.F.: The temperature of rubbing surfaces. Wear **2**(6), 438–455 (1959). https://doi.org/10.1016/0043-1648(59)90159-0
41. Evans, C.R., Johnson, K.L.: Regimes of traction in elastohydrodynamic lubrication. Proc. Inst. Mech. Eng., Part C: J. Mech. Eng. Sci. (1986). https://doi.org/10.1243/PIME_PROC_1986_2
42. Loewenthal, S.H., Rohn, D.A.: Elastic model of the traction behavior of two traction lubricants. ASLE Trans. **27**(2), 129–137 (1984). https://doi.org/10.1080/05698198408981553
43. Bair, S., Flores-Torres, S.: The viscosity of polyalphaolefins mixtures at high pressure and stress. J. Tribol. **141**(2), 1–7 (2019). https://doi.org/10.1115/1.4041124

Publisher's Note Springer Nature remains neutral with regard to jurisdictional claims in published maps and institutional affiliations.

Authors and Affiliations

Alexander MacLaren[1] · Amir Kadiric[1]

✉ Alexander MacLaren
dam216@ic.ac.uk

Amir Kadiric
a.kadiric@imperial.ac.uk

[1] Department of Mechanical Engineering, Imperial College London, Exhibition Road, London SW7 2AZ, UK